Alma Mater Studiorum · Università di Bologna

Corso di Laurea Magistrale in Chimica Industriale
Classe LM-71 - Scienze e Tecnologie della Chimica Industriale

Modeling Ultrafast Spectroscopy of the NADH Dimer From UV-VIS to X-rays

Candidato:
Francesco Montorsi

Relatore:
Prof. Marco Garavelli

Co-relatore:
Dott. Francesco Segatta

I Sessione
Anno Accademico 2021-2022

Contents

Abstract

Ultrafast pump-probe spectroscopy is a conceptually simple and versatile tool for resolving photoinduced dynamics in molecular systems. Due to the fast development of new experimental setups, such as synchrotron light sources and X-ray free electron lasers (XFEL), new spectral windows are becoming accessible. On the one hand, these sources have enabled scientist to access faster and faster time scales and to reach unprecedent insights into dynamical properties of matter. On the other hand, the complementarity of well-developed and novel techniques allows to study the same physical process from different points of views, integrating the advantages and overcoming the limitations of each approach. In this context, it is highly desirable to reach a clear understanding of which type of spectroscopy is more suited to capture a certain facade of a given photo-induced process, that is, to establish a correlation between the process to be unraveled and the technique to be used. In this thesis, I will show how computational spectroscopy can be a tool to establish such a correlation. I will study a specific process, which is the ultrafast energy transfer in the nicotinamide adenine dinucleotide dimer (NADH). This process will be observed in different spectral windows (from UV-VIS to X-rays), accessing the ability of different spectroscopic techniques to unravel the system evolution by means of state-of-the-art theoretical models and methodologies. The comparison of different spectroscopic simulations will demonstrate their complementarity, eventually allowing to identify the type of spectroscopy that is best suited to resolve the ultrafast energy transfer.

Chapter 1

Introduction

Photo-induced events are of upmost importance in our life. They are at the foundation of the photosynthetic process that provides us oxygen and other chemical compounds that are key for the existence and persistence of life on earth. Humans and animals are able to see the word which surrounds them as a manifestation of the light-matter interaction which take place in their eyes.
The above examples involve specific molecules or molecular aggregates which are able to absorb and temporarily harvest the energy of light and to exchange or to utilize it for specific functions. The extreme efficiency of such natural processes are nowadays of great interest for the scientific community, that seek to understand how to build novel solar energy technologies in order to overcome the current energy crisis.
The experimental investigation of such events, poses several challenges and it is usually achieved by means of ultrafast spectroscopic techniques. The time scales of common photo-induced events, in fact, are typically very short (from tens of femtoseconds to few picoseconds) and for such reason high time resolution is required to track the light-induced perturbation of the molecular system. In the last few decades, such experiments have allowed the successful investigation of some fundamental processes involved in the human vision[1], in the working principles of some photosynthetic complexes[2], and in countless other areas of research. Still, some challenging problems remain unsolved, and an integrated theoretical and experimental approach is called for. In particular, common ultrafast experiments are usually congested of information which are hard to be extracted and disentangled. In order to get a clear understanding of the experimental results robust and reliable theoretical models have to be developed for the description of the system[3].

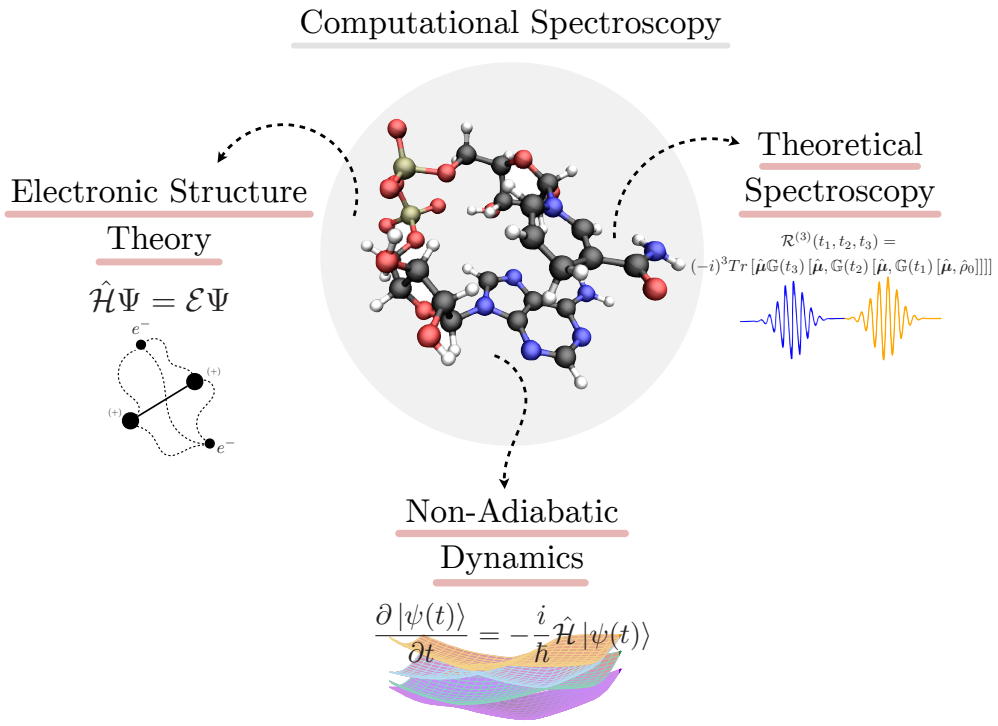

Figure 1.1: Pictorial representation of the three theoretical pillars that sustain the simulation of ultrafast spectroscopy.

From a computational point of view modeling ultrafast spectroscopy requires[4]: (a) an accurate description of the molecular system under scrutiny which is typically provided by electronic structure theory; (b) a way to account for the dynamic response of the system to light, which is achieved, in general, by means of non-adiabatic molecular dynamics; (c) a way to describe the light-matter interaction occurring in the spectroscopic experiment under scrutiny. In this thesis the so-called *response function* approach firstly introduced by Prof. Shaul Mukamel a few decades ago[5] is the way used to tackle this problem. A pictorial representation these three theoretical pillars is given in Fig. 1.1.

Due to the recent development of new experimental setups, such as synchrotron light sources and X-ray free electron laser (XFEL), new experimental techniques are becoming accessible enabling, scientist to probe faster and faster time-scales.

In this context, theoretical chemistry can assume a slightly different role that of interpreting experimental results, and can be used to anticipate the experiments which are still unfeasible with the current technologies, facilitating the development of new spectroscopic techniques[6, 7]. X-rays based techniques are also gaining increasing interest in the field of ultrafast spectroscopy due their ability to probe the evolution of the system in a local fashion, achieving structural insights inaccessible in other spectral windows[8, 9].

The aim of this thesis is to investigate, from the theoretical point of view, the complementarity of well-developed and novel spectroscopic techniques, trying to reach a clear understanding of which type of spectroscopy is more suited to capture a certain facade of a given photo-induced process and establishing a correlation between the process to be unraveled and the technique to be used to unravel them. This thesis is organized as follows:

- Part 1 is focused on the phenomenological and theoretical description of electronic spectroscopy. The characteristic features of different electronic spectroscopies are outlined and the perturbative response function approach for the simulation of ultrafast spectroscopy is introduced.

- Part 2 is focused on electronic structure theory and on the theoretical methodologies used to the describe both static and dynamic properties of molecular systems. A particular attention is reserved to the modeling of molecular vibration, their coupling to the electronic transitions of interest, and their impact on the simulated spectra.

- Part 3 presents the results obtained on the NADH dimer, a biologically relevant cromophore characterized by an intriguing and not completely understood photo-physics. Here simulations of different ultra-fast techniques are reported, and their ability to resolve the photo-physics of NADH is discussed. In particular, the well-established UV-VIS *pump-probe* technique is simulated starting from mechanistic insights obtained by previous quantum dynamical study performed in collaboration with Dott. Fabrizio Santoro

(CNR Pisa) and the results of the simulations are compared to the new experimental results obtained in the group of Prof. Giulio Cerullo (Politecnico di Milano).
Simulations of different ultrafast techniques are then showed, namely: TR-PES, TR-NEXAFS and TR-XPS. Their ability to resolve the photo-physics of NADH is eventually discussed.

Part I

Phenomenology and Theory of Electronic Spectroscopy

Chapter 2

Electronic spectroscopy: a bird's-eye view

Spectroscopy is a widely employed and well developed tool that uses light to study the properties of matter. From a very general point of view, it requires the presence of a source of electromagnetic radiation (typically a laser) which illuminates a sample containing the system of interest (e.g., some biological cromophores) and a detector which is able to collect the response of the system to light-induced perturbations. A wide variety of processes can be triggered by light of different wavelength and intensity, requiring different detection techniques, and defining the different spectroscopic techniques. In this thesis we will focus on electronic spectroscopy of molecules, for which the electromagnetic radiation is resonant with the electronic transitions of the molecular system.

Spectroscopic techniques can be also classified according to the characteristic of the radiation source: in particular we distinguish steady state form time resolved spectroscopy. In the first, the sample is continuously irradiated, and excited states of the system are created and annihilated until a steady-state is reached and their concentration remain constant. This provides a high sensitivity to the energetic positions and probabilities of the observed electronic transitions. The second, at variance, relies on the irradiation of the sample by pulsed light which is able to create a burst of excited states whose evolution is monitored with a second beam of light as a function of time. This provide kinetic information about the system like lifetimes and the fate of a given excited states.

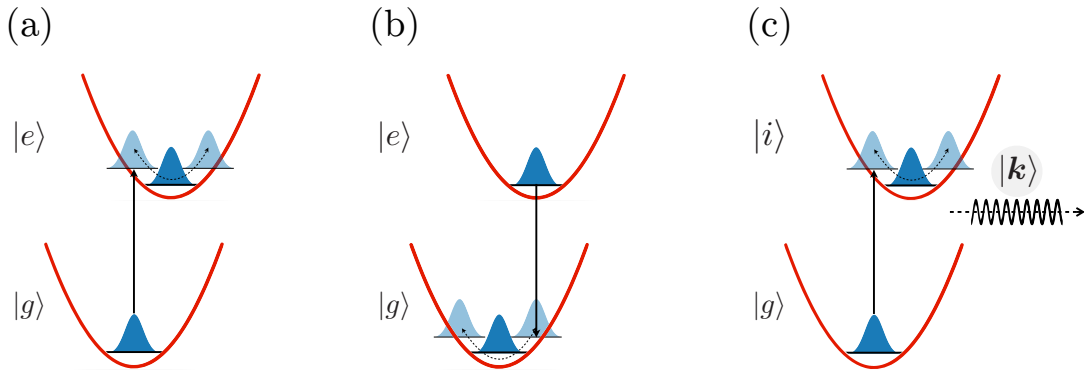

Figure 2.1: Schematic representation of: (a) absorption process from the ground state $|g\rangle$ to the excited state $|e\rangle$; (b) spontaneous emission process from $|e\rangle$ to $|g\rangle$; (c) photo ionization process from $|g\rangle$ to the cationic state $|i\rangle$ with the simultaneous emission of a photoelectron $|\boldsymbol{k}\rangle$.

2.1 Linear Absorption, Emission and Photoelectron techniques

Linear absorption techniques measure the fraction of light absorbed by a sample irradiated by a continuous wave beam of light. The absorbed light promotes the system to an excited state, giving information about the energy difference between the ground and the excited states. The probability to populate a given excited state is related to the its nature, and thus, each electronic transition is characterized by different probability to occur according to the so-called optical selection rules. If a given electronic transition fulfills the aforementioned rules, the excitation process can take place with a probability related to the transition dipole moment matrix element ($\boldsymbol{\mu}$) between the initial and the final state.

Emission techniques measure the electromagnetic radiation emitted upon the deactivation of the excited states. The recorded emission spectra provides information about excited-state lifetimes. The emission yield is again related to transition dipole moment between the excited and ground state.

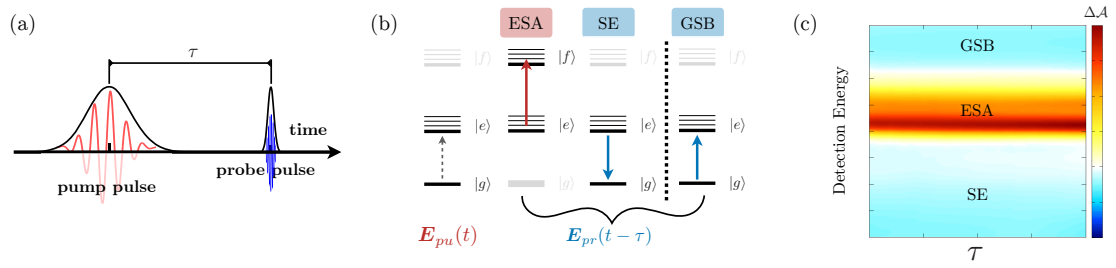

Figure 2.2: (a) Pictorial representation of the PP pulse scheme. (b) Level diagrams of the different processes which occur in PP spectroscopy. (c) Example of a $\Delta\mathcal{A}(\omega, \tau)$ map.

Photo-electron techniques, at variance, relies on the famous photoelectric effects. Here the sample is irradiated by a continuous wave beam of (almost) monochromatic light which is able to promote the system to a cationic state with the simultaneous ejection of a "photo-electron" into the continuum. The final photo-electron spectra is then recorded collecting the outgoing photo-electrons (e.g with a magnetic bottle trap) and measuring their kinetic energy (and also their angular distribution, in the most refined experiments). This technique provides information about the binding energy of the electrons in a given molecular system.

2.2 Pump-Probe Spectroscopy

The ultrafast photo-induced processes which occur in nature require time resolved techniques to be investigated. In this context, *pump-probe* (PP) spectroscopy is a conceptually simple, but versatile, tool to resolve the coupled electron-nuclear dynamics of molecules subjected to photo excitation. In this thesis different flavors of the same technique are studied, where each of them is characterized by different peculiarities as well as by different advantages in the study of a given photo-induced event. In the following we present qualitatively the setup and the processes which occur in typical PP experiment.

In PP experiment a first strong pulse (called *pump*) prepares the system in an

excited state while a second weaker pulse (called *probe*) monitors the evolution of the system after a given time delay τ. The absorption spectrum $\mathcal{A}(\omega, \tau)$ of the sample is recorded for each given time delay τ and the final spectra is obtained as a differential signal $\Delta\mathcal{A}(\omega, \tau)$, subtracting to $\mathcal{A}(\omega, \tau)$ the absorption of the system in ground state (i.e. the absorption spectra of the sample only subjected to *probe* pulse). This procedure is repeated for several values of τ and the results are typically organized as a two dimensional time-frequency map (as reported in figure 2.2-(c)). The response of the excited system to the probe pulse comes from different processes (schematically depicted in Fig 2.2-(b)):

1. **G**round **S**tate **B**leacing (GSB) contributions: The fraction of molecules which are still in the GS after the *pump* pulse has passed through the sample, is smaller than the total number of molecules. As a consequence, the ground state absorption of the previously pumped system is quenched. This leads to a negative signal in the $\Delta\mathcal{A}(\omega, \tau)$ map which is observed in the energy reagion of the ground state absorption.

2. **S**timulated **E**mission (SE) contributions: This process is triggered when a photon of the *probe* induces the deactivation of those molecules previously excited by the *pump* pulse. As a consequence, a second photon is emitted from the system leading to an increasing of the light intensity recorded by the detector corresponding to a negative signal in the $\Delta\mathcal{A}(\omega, \tau)$ map. Such kind of signal resemble the spectral profile obtained recording the spontaneous emission of the excited cromophore.

3. **E**xcited **S**tate **A**bsorption (ESA) contributions: the excited molecules created by the absorption of the *pump* pulse can be themselves excited to higher-lying states by the *probe* pulse. As a consequence, an absorption signal is recorded which correspond to a positive contribution to the total $\Delta\mathcal{A}(\omega, \tau)$ map.

Typical photo-induced events in nature take place in time scales ranging from tens of femtoseconds (fs) to a few nanoseconds (ns). In this context, the control over

the time delay τ and over the pulse duration is of upmost importance. The latter, in particular puts a strong limit to the time resolution achievable in a given transient absorption experiment which can be at most equal to the time duration of the laser pulses. Extremely short pulses are thus able to provide equally high time resolutions but at the cost of a reduced spectral sensitivity since the time bandwidth product relation prohibits the spectral bandwidth to be arbitrary small ($\Delta w \Delta t \sim$ const).

Finally, the control over the relative polarization of the pulses can be used to enhance or to quench different contributions in the total spectrum, providing additional information about the system under scrutiny.

2.2.1 Excited states notation

In PP experiments different excited state of the system can be created by the interaction with the two pulses. The nature of these excited states might depend on the employed spectroscopic technique. Nonetheless, they are typically partitioned in different manifolds according to their energy.

In general the first excited state manifold is called e-manifold ($|e\rangle$) and collects all the states directly accessible during the interaction with the first pulse (i.e all the states which are resonant within the bandwidth of the *pump*). The second excitation manifold, at variance, is called f-manifold ($|f\rangle$) and gather the higher lying states responsible for the ESA contributions (i.e resonant within the bandwidth of the *probe*). The same notation will be applied in the following chapters where we develop the theoretical formalism for the spectroscopy simulation.

2.2.2 Two-Window Experiments

The *traditional* PP experiment described above can be also called one-color experiment since the carrier frequency of the pump field and that of the probe field are in the same spectral window. However, monitoring the evolution of a given

excited state using light of different energy (i.e. with a probe pulse belonging to a different spectral window) can provide additional information on the pump-induced dynamics, integrating the advantages and overcoming the limitations of the one-color approach. Such kind of techniques are called two-color experiments and they will play an important role in this thesis.

2.3 Description of electronic processes

In the last section we introduced the idea to probe a given photo-induced event using pulses from different spectral windows. In particular, in this work, we will study electronic spectroscopy curried out using light from the UV-VIS to the X-rays. A large number of processes can occur when light in such a wide energy range interact with the molecular system, and most of them go beyond the aim of this work. We will focus in particular on photo-excitation in the UV-VIS and X-rays window and on photo-ionization in the EUV and X-rays window. A schematic description of these processes is given in figure 2.3.

2.3.1 UV-VIS window: UV-VIS spectroscopy

As a consequence of the absorption of a UV-VIS photon an electron is usually promoted from a doubly occupied valence orbital to a virtual orbital and the excited state that are populated in this way are called *valence*-excited states.
The spectrum of solar radiation (on Earth) is dominated by photons belonging to the VIS/UV spectral window and, for such reason, the common photo-chemical and photo-physical processes which occur in nature involve these states. Since one of the goals of time resolved techniques is to study such kind of processes most of them use UV/VIS *pump* pulses which we will refer to as optical pulses.

If, after the optical excitation, a second *probe* pulse in the optical regime is employed to study the evolution of the system, the corresponding TR technique is simply the widely employed one-color PP technique discussed in the previous sections. In the following parts of this work we will refer to it as the PP experiment.

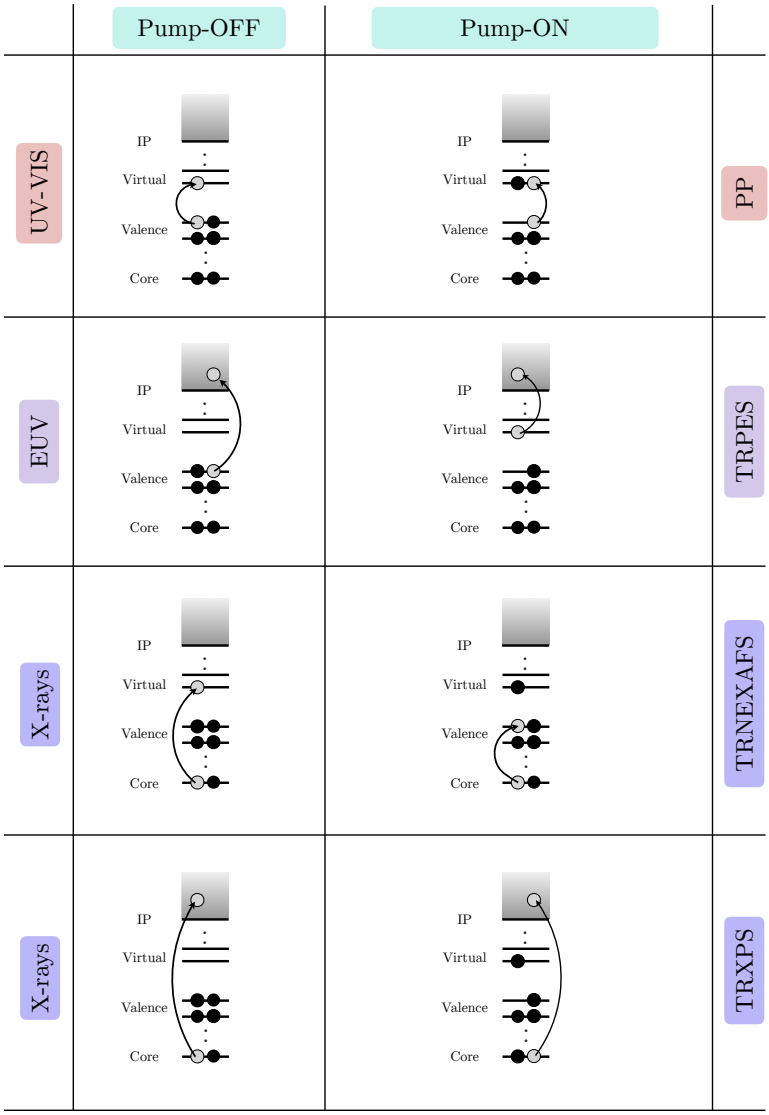

Figure 2.3: Schematic representation of the different electronic processes discussed in this thesis. The rows highlight the electronic transitions triggered by light belonging to different spectral windows (from UV-VIS to X-rays) while the two central columns shows the excitation/ionization processes that occur in the PUMP-OFF and PUMP-ON conditions. The extra columns labels the energy windows (left) and the names of the respective techniques (right).

2.3.2 EUV window: PES spectroscopy

In the EUV window, the high energy electromagnetic radiation is capable to promote an electron from a doubly occupied valence orbital into the continuum, i.e to ionize the molecular system. The process produce a bound ionic state (that we will call a valence-ionized state), and a free photoelectron whose kinetic energy is eventually measured. The resulting photoelectron spectra (PES) collects information about the binding energies of the electrons hold in different valence orbitals (BE = Pulse energy - electron kinetic energy). When the *valence* photoionization process is used to probe a dynamics initiated by a UV-VIS pulse, the resulting technique is called Time Resolved PhotoElectron Spectroscopy (TRPES) and its sensitivity to both electronic and nuclear configuration is known since the development of the first gas phase experiment in the early 1980s[10]. Nowadays, thanks to the recent employment of the liquid microjet technology[11], TRPES experiments in water solutions are also possible, enabling the possibility to study biologically relevant crhomophores in their realistic environment[12].

Valence-excited states in the TRPES are visualized with signals which appears in a background free region red shifted from the ground-state absorption region. In fact, after the pump-induced excitation of the system, an electron can be found in an higher lying molecular orbital (e.g. the LUMO of the system) and its ionization leads to a red shifted signal which is a unique fingerprint of the excited state. This, in principle, enables to study photo-induced events without any background signal coming from the GS which can spoil the information content of the experiment.

In the previous sections, the nomenclature of the characteristic PP signals have been introduced. In the context of TRPES however is not correct to use the same notation. For this reason, we will use **G**round **S**tate **I**onizzation (GSI) to describe the ionization of the that fraction of molecules which is still in the ground state after the optical *pump* while we will call **E**xcited **S**tate **I**onizzation (ESI) when the ionized molecule are located in an excited state.

2.3.3 X-ray window: NEXAFS spectroscopy

In contrast with the optical regime, which involve only valence orbitals, the absorption of an X-ray photon promotes a core electron to a virtual orbital. As a consequence, the system is brought to an excited state which is called *core*-excited state. In particular, if the absorption process is measured below the ionization potential of the excited core orbital, the corresponding experimental technique is called Near Edge X-ray Absorption Spectroscopy (NEXAFS). NEXAFS is a rich experimental technique characterized by different kinds of possible signals according to the type of core orbital which is excited. We call *edges* the energy region of the spectra where the ionization process of a given core orbital begins and we use this terminology to classify the X-ray window of interest. In particular, the *edges* are classified according to the principal quantum number (n) of the excited core orbital. For $n = 1$ the core orbitals involved in the excitation process are the 1s orbitals and the corresponding technique is called K-*edge*. Different *edges* follow the K-*edge* for increasing values of n, such as the L-*edge* ($n = 2$) and the M-*edge* ($n = 3$) just to name a few.

Even if X-rays have been known by almost a century for their ability of studying the properties of matter, the recent interest of the scientific community in the use of X-ray spectroscopy to study photo-induced event, however, is not immediately clear. In fact, chemistry happens entirely in the valence shell. Valence electron are directly responsible for the interaction between the atoms forming a molecule and they are also responsible for the molecular excitation occurring in nature. In fact, since they are only weakly attached to positive nuclei, they can be displaced or even be transfer after the excitation process, thus leading to rich and interesting photo-chemical and photo-physical behaviors.
Core (or inner-shell) electrons are firmly attached to the nuclei and their main activity in the molecular system is to shield the positive charge of the nuclei forming the molecule. In this picture core electrons look only as *spectators* since they are simply unable to participate to what is happening in the outermost region of the system. Although this statement is true, core electrons feel the potential of

the valence electron and thus, they are sensitive to perturbations in the outermost shells.
In this context, monitoring photo-induced events by the means of X-ray spectroscopy provides local information about the time dependent electronic structure of a system, thanks to same unique features of the core excitations, that we briefly summarize hereafter:

- **Element resolution:** Different elements experience nuclear potentials which increase directly with the atomic number Z. Due to this fact, excite the same 1s core electron of an higher Z atom costs more energy compared to an atom with a lower Z. For this reason the energy window where the transitions of a given element fall are about 100 eV shifted compared to the transitions of its direct neighbors in the periodic table. This feature enables to study individually the transitions coming from a specific element of the system and the corresponding window is called *element* K-*edge* (e.g. carbon K-*edge*).

- **Atomic resolution:** The same element but subjected to different local chemical environment experience a different potential due to the different distribution of the electronic density in the outer shell. This enable to identify the individual NEXAFS contribution of atoms in different chemical environment delivering local information on the electronic structure of the system. However, for system with a lot of similar atoms this kind of resolution might not be accessible.

- **Excited state resolution:** Exciting a given *valence*-excited state changes the molecular electron density (such in the case reported in ref. [13]). The response of the core electrons when this molecule is in a valence excited-state will thus be different to their response when the system is in the ground state. This, in principle, enable to monitor the light induced electronic structure modification obtaining, at the same time, local information about the nature of the populated excited state. Furthermore, the previously prepared excited state has now an hole in a valence orbital (e.g. the HOMO of the system) which can be filled by the core electron promoted by the incoming X-ray field.

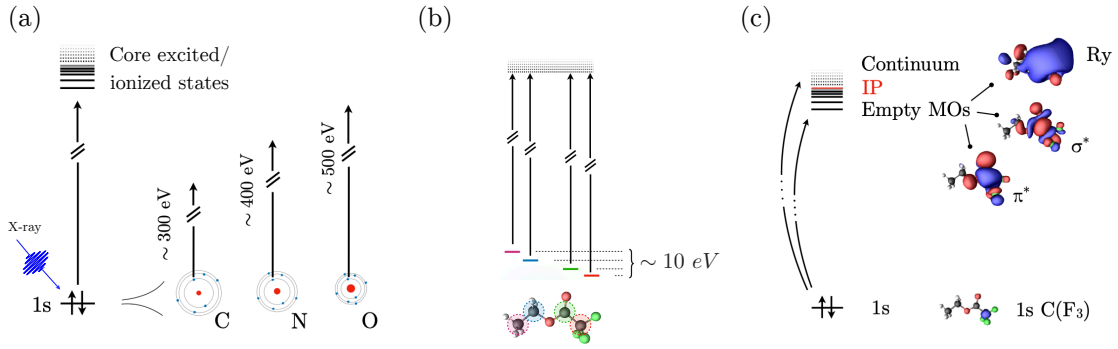

Figure 2.4: Representation of element (a) and atomic (b) resolutions achievable with X-ray spectroscopy. (c) Schematic of the shows the different *resonances* which characterize the NEXAFS, namely π^*/σ^*/Rydberg-*resonances*.

If this transition is bright, a new signal related to such an excited state would appear red-shifted background free region, in analogy with TRPES.

Schematic description of such properties are reported in figure 2.4-(a)&(b). Using a molecular orbital based description of the excitation process, we can easily classify the various kind of core excited states according to the virtual orbital in which the core electron is relocated:

- π^*-***resonance***: These transition are present for such molecules with a π system and, if they are present, they are typically the lower energy, and the strongest, transitions of the NEXAFS spectra[1].
- ***Rydberg***(Ry)-***resonance***: They are commonly placed between the π^*-*resonances* and the ionization potential. They typically are narrow, low intensity features corresponding to the filling of an highly diffuse Rydberg type orbital. Due to the destabilization of Ry type orbital in solution[2] this kind of features are commonly absent when the NEXAFS experiment is performed out in solution.

[1]Which is however characterized by a very low intensity compared to a common UV-VIS spectra.

[2]Since they are highly diffuse orbitals, they strongly interact with the electronic density of the solvent leading to a global destabilization of the corresponding excited state.

- σ^*-***resonance***: They are usually the higher energy signal of NEXAFS spectra and according to the nature of the atoms involved in the σ bond they can be found below or above the ionization potential. If their excitation energy is higher than the IP the nature of the corresponding core-excited states are *semi-bound*. This means that, the excited states populated in this way is a *meta-stable* states, which suddenly undergo *auto*-ionization. Due to this fact, the common band width of such *resonances* is extremely large, due to the very short state life-time.

- ***Shake-up Satellites*** (Su): Finally, this signal is recorded when a given valence excitation happens at same time of a given core excitation. These are two-electron processes and, for such reason, they are in principle dark[3]. However, due to the multi-configurational nature of the excited states, also this kind of processes might acquire some brightness which is typically one order of magnitude lower than the one of the main signal (i.e. the signal produced by single electron core excitations). Such shake-up states are usually visualized as low intensity satellites of the main band.

2.3.4 X-rays window: XPS spectroscopy

The analog of PES measured in the X-ray window is called X-ray Photoelectron Spectroscopy (XPS) and involve the ionization of core orbitals. This techniques is conceptually simpler compared to NEXAFS since each element of the system contributes to the total spectrum only with a main signal and with one shake-up satellite. This simplicity can became an advantage in the case of Time Resolved XPS (TRXPS) compared to Time Resolved NEXAFS (TRNEXAFS), where a less congested spectrum can deliver more clear information.

[3]This because the transition dipole moment operator is a one-electron operator.

Chapter 3

Models of Theoretical Spectroscopy

The microscopic understanding of spectroscopic phenomena requires strong models capable to describe the light-matter interaction. From a theoretical point of view the physics of a given photo-induced process (such as spectroscopy) is entirely encoded into the so called *field-matter* Hamiltonian which reads:

$$\hat{\mathcal{H}} = \hat{\mathcal{H}}_0 + \hat{\mathcal{H}}'(t) \tag{3.1}$$

where $\hat{\mathcal{H}}_0$ is the time independent Hamiltonian of the *matter* (i.e. the molecular system) while $\hat{\mathcal{H}}'(t)$ is the time dependent interaction between the external EM field and the *matter*. For the moment, we give no information about the nature of $\hat{\mathcal{H}}_0$, the modeling of which will be discussed in next part of the thesis.
In this work we treat the interaction term $\hat{\mathcal{H}}'(t)$ within the semi-classical ansatz, for which the molecular system interact with a classical EM field $\boldsymbol{\mathcal{E}}(\boldsymbol{r}, t)$ via dipole interaction (dipole approximation):

$$\hat{\mathcal{H}}'(t) = -\hat{\boldsymbol{\mu}} \cdot \boldsymbol{\mathcal{E}}(\boldsymbol{r}, t) \tag{3.2}$$

where $\hat{\boldsymbol{\mu}}$ is the dipole operator of the molecular system, and $\boldsymbol{\mathcal{E}}(\boldsymbol{r}, t) = \mathcal{E}(t)e^{-\boldsymbol{k}\cdot\boldsymbol{r}-i\omega t}$ is the classical electromagnetic field of the laser, with time envelope $\mathcal{E}(t)$ and wave-vector $\boldsymbol{k}$.

A non stationary quantum state $|\psi(t)\rangle$ evolves in time following the time dependent Schrödinger equation (TDSE):

$$\frac{\partial}{\partial t}|\psi(t)\rangle = -\frac{i}{\hbar}\hat{\mathcal{H}}|\psi(t)\rangle \tag{3.3}$$

From a theoretical point of view, it is thus possible to describe any kind of *field-matter* interaction problem just defining the Hamiltonian as in Eq. 3.1 and solving

the TDSE. The various kinds of spectroscopic experiments discussed in the previous chapter would then be obtained computing the polarization induced in the sample by the external field[1], which is the expectation value of the dipole moment operator $\hat{\boldsymbol{\mu}}$.
However the brute force solution of the TDSE is not practically feasible for many systems of interest (such as molecules with hudreds of atoms in a complex environment) witout some approximations. To overcome this issue time-dependent perturbation theory is commonly employed. In this framework the n-th order expansion of the interaction term $\hat{\mathcal{H}}'(t)$ correspond to a scenario where the EM field interacts n times with the molecular system. Different orders of the perturbative expansion than give rise to different spectroscopic techniques. For the purpose of this thesis only first and third order terms (corresponding to linear and PP techniques respectively) will be discussed.

In this context a density matrix representation of the problem is usually preferred to a wave-function based approach since it is the natural formulation of open quantum system problems.
Open quantum systems (OQS) are the physical way to describe large QM systems such as molecules in solution and they require a formalism able to model statistical ensembles of states[2] and dissipation processes.

3.1 Perturbative treatment of the field-matter interaction

The density operator (or density matrix) of the system is defined as:

$$\hat{\rho}(t) = |\psi(t)\rangle \langle\psi(t)| \tag{3.4}$$

Using the TDSE (and knowing that $\hat{\mathcal{H}} = \hat{\mathcal{H}}^{\dagger}$) both the time evolution of the *ket*

[1] As we will see, the polarization is the source of the signal.

[2] A wave function based description of the system is only able to describe coherent superposition of states but not a "mixture" of states.

$|\psi(t)\rangle$ and of the *bra* $\langle\psi(t)|$ can be described as:

$$\frac{\partial}{\partial t}|\psi(t)\rangle = -\frac{i}{\hbar}\hat{\mathcal{H}}|\psi(t)\rangle \tag{3.5}$$

$$\frac{\partial}{\partial t}\langle\psi(t)| = +\frac{i}{\hbar}\langle\psi(t)|\hat{\mathcal{H}} \tag{3.6}$$

the time evolution of the density matrix can therefore be written as:

$$\frac{\partial}{\partial t}\left(|\psi(t)\rangle\langle\psi(t)|\right) = -\frac{i}{\hbar}\hat{\mathcal{H}}|\psi(t)\rangle\langle\psi(t)| + \frac{i}{\hbar}|\psi(t)\rangle\langle\psi(t)|\hat{\mathcal{H}} \tag{3.7}$$

$$\frac{\partial}{\partial t}\hat{\rho}(t) = -\frac{i}{\hbar}\left[\hat{\mathcal{H}}, \hat{\rho}(t)\right] \tag{3.8}$$

Eq. 3.8 describe the time evolution of the density operator and is called *Liouville-von Neumann* (LVN) equation. Formal integration of the LVN leads to:

$$\hat{\rho}(t) = \hat{\rho}_0(t) - \frac{i}{\hbar}\int_{t_0}^{t}\left[\hat{\mathcal{H}}, \hat{\rho}(t)\right] \tag{3.9}$$

which can be solved iteratively by plugging it into itself:

$$\hat{\rho}(t) = \hat{\rho}(t_0) + \sum_{n=1}^{+\infty}\left(-\frac{i}{\hbar}\right)^n \int_{t_0}^{t} d\tau_n \int_{t_0}^{\tau_n} d\tau_{n-1} \cdots \int_{t_0}^{\tau_2} d\tau_1 \left[\hat{\mathcal{H}}(\tau_n), \left[\hat{\mathcal{H}}(\tau_{n-1}), \cdots \left[\hat{\mathcal{H}}(\tau_1), \hat{\rho}(t_0)\right] \cdots\right]\right] \tag{3.10}$$

which is a series expansion in terms of $\hat{\mathcal{H}}$. One would be tempted to truncate this expansion to a finite order: since $\hat{\mathcal{H}}$ is not a perturbation, this is not doable, and the brute force integration of equation 3.8 is required. The interaction term $\hat{\mathcal{H}}'(t)$, at variance, is typically small and, for this reason, recasting equation 3.10 only in terms of $\hat{\mathcal{H}}'(t)$ will provide the possibility to truncate the aforementioned series. In order to do that, we introduce the *interaction picture representation*[14] for which the density matrix and the perturbative Hamiltonian reads:

$$\hat{\rho}_I(t) = \mathbb{G}(t)\hat{\rho}(t) \tag{3.11}$$

$$\hat{\mathcal{H}}'_I(t) = \mathbb{G}(t)\hat{\mathcal{H}}'(t) \tag{3.12}$$

where the $\mathbb{G}(t)$ is superoperator defined as $\mathbb{G}(t)\hat{A} = e^{-\frac{i}{\hbar}\hat{\mathcal{H}}_0 t}\hat{A}\ e^{\frac{i}{\hbar}\hat{\mathcal{H}}_0 t}$ and basically describes the so called field-free evolution operator $\hat{A}$. If $\hat{A} = \hat{\rho},\ G(t)\rho$ describes i.e the evolution of the system subjected only to the molecular Hamiltonian $\hat{\mathcal{H}}_0$. Recasting Eq. 3.10 within this representation leads to:

$$\hat{\rho}(t) = \hat{\rho}_I(t_0) + \sum_{n=1}^{+\infty}\left(-\frac{i}{\hbar}\right)^n \int_{t_0}^{t} d\tau_n \int_{t_0}^{\tau_n} d\tau_{n-1}\ \cdots \int_{t_0}^{\tau_2} d\tau_1 \\ \left[\mathbb{G}(t-\tau_n)\hat{\mathcal{H}}'_I(\tau_n), \left[\mathbb{G}(\tau_n-\tau_{n-1})\hat{\mathcal{H}}'_I(\tau_{n-1}),\ \cdots \left[\mathbb{G}(\tau_1)\hat{\mathcal{H}}'_I(\tau_1), \hat{\rho}(t_0)\right]\ \cdots\right]\right] \tag{3.13}$$

Now, assuming $\hat{\mathcal{H}}'(t)$ to be week perturbation we can truncate the series obtaining the corresponding perturbative expression of the density matrix at the generic n-th order as:

$$\hat{\rho}^{(n)}(t) = \left(-\frac{i}{\hbar}\right)^n \int_{t_0}^{t} d\tau_n \int_{t_0}^{\tau_n} d\tau_{n-1}\ \cdots \int_{t_0}^{\tau_2} d\tau_1 \\ \left[\mathbb{G}(t-\tau_n)\hat{\mathcal{H}}'_I(\tau_n), \left[\mathbb{G}(\tau_n-\tau_{n-1})\hat{\mathcal{H}}'_I(\tau_{n-1}),\ \cdots \left[\mathbb{G}(\tau_1)\hat{\mathcal{H}}'_I(\tau_1), \hat{\rho}(t_0)\right]\ \cdots\right]\right] \tag{3.14}$$

During the light-matter interaction, the incoming field perturbs the charges of the sample molecules giving thus rise to a time-dependent polarization which is, itself, a source of a new oscillating field. The incoming EM radiation can thus interfere with this new field giving rise to the measured signal. For this reason the induced polarization $\boldsymbol{\mathcal{P}}(t)$ is the quantity of interest for the modeling of spectroscopic signals.

The n-th order of the photo-induced polarization $\boldsymbol{\mathcal{P}}^{(n)}(t)$ is given by the expectation value of the dipole operator as:

$$\boldsymbol{\mathcal{P}}^{(n)}(t) = Tr\left[\hat{\boldsymbol{\mu}}\hat{\rho}^{(n)}(t)\right] \tag{3.15}$$

combining then this equation with equation 3.14, and specifying the nature of the perturbation (i.e $\hat{\mathcal{H}}'(t) = -\boldsymbol{\mathcal{E}}(t)\cdot\hat{\boldsymbol{\mu}}$), the induced polarization becomes:

$$\begin{aligned}\boldsymbol{\mathcal{P}}^{(n)}(t) = \left(-\frac{i}{\hbar}\right)^n \int_0^{+\infty} dt_n \int_0^{+\infty} dt_{n-1} \ \cdots \ \int_0^{+\infty} dt_1 \ \boldsymbol{\mathcal{E}}(\boldsymbol{r}, t - t_n) \\ \boldsymbol{\mathcal{E}}(\boldsymbol{r}, t - t_n - t_{n-1}) \cdots \boldsymbol{\mathcal{E}}(\boldsymbol{r}, t - t_n - t_{n-1} \cdots - t_1) \\ Tr\left[\hat{\boldsymbol{\mu}}\mathbb{G}(t_n), [\hat{\boldsymbol{\mu}}\mathbb{G}(t_{n-1}), \ \cdots \ [\hat{\boldsymbol{\mu}}\mathbb{G}(t_1), [\hat{\boldsymbol{\mu}}, \hat{\rho}_0]] \ \cdots \ ]\right] \end{aligned} \tag{3.16}$$

where we have defined the equilibrium density matrix as $\hat{\rho}_0$. We have also used a different sets of time variables in the integrals defined as:

$$\begin{aligned}\tau_1 &= 0 \\ t_1 &= \tau_2 - \tau_1 \\ t_2 &= \tau_3 - \tau_2 \\ &\vdots \\ t_n &= t - \tau_n\end{aligned}$$

In the next sections we will finally connect the n-th order polarization with the corresponding measured signals.

3.2 Linear and PP signals

It is possible to show that linear absorption signal ($\mathcal{W}^{(1)}(\Omega_1)$) the Fourier Transform (FT) of the fist order polarization[14]:

$$\mathcal{W}^{(1)}(\Omega_1) = \int_0^{+\infty} dt_1 \boldsymbol{\mathcal{P}}^{(1)}(t_1) e^{i\Omega_1 t_1} \tag{3.17}$$

where $\boldsymbol{\mathcal{P}}^{(1)}(t_1)$ can be derived by the general expression of the n-th order polarization discussed above and reads:

$$\boldsymbol{\mathcal{P}}^{(1)}(t_1) = \int_0^{+\infty} dt_1 \mathcal{R}^{(1)}(t_1) \mathcal{E}(t - t_1) \tag{3.18}$$

In this expression $\mathcal{R}^{(1)}(t_1)$ is the so-called *response function*, which encodes the effect of the first order light-induced perturbation of the system. Looking at Eq. 3.16 the first order response function can be rewritten as:

$$\mathcal{R}^{(1)}(t_1) = \left(-\frac{i}{\hbar}\right) Tr\left[\hat{\boldsymbol{\mu}}\mathbb{G}(t_1)\left[\hat{\boldsymbol{\mu}}, \hat{\rho}_0\right]\right] \tag{3.19}$$

In analogy with Eq. 3.17 we can define the PP signal $\mathcal{W}^{(3)}(t_2, \Omega_3)$ as the marginal of the Fourier Transform of the third-order polarization[14]:

$$\mathcal{W}^{(3)}(t_2, \Omega_3) = \int_{-\infty}^{+\infty} dt_1 \int_0^{+\infty} dt_3 \; \boldsymbol{\mathcal{P}}^{(3)}(t_1, t_2, t_3) e^{i\Omega_3 t_3} \delta(t_1) \tag{3.20}$$

The general formalism behind the third-order polarization involve the interaction of the system with three incident laser pulses respectively with wave vectors $\boldsymbol{k}_1$, $\boldsymbol{k}_2$ and $\boldsymbol{k}_3$ and with time delays t_1, t_2 and t_3. Practically, experiments can be curried out also by means of only two pulses (i.e., the *pump* and *probe*) assuming that the *pump* pulse interacts twice with the system. From a formal point of view this corresponds to assume short t_1 time delay ($t_1 \simeq 0$). The third-order polarization reads:

$$\begin{aligned}\boldsymbol{\mathcal{P}}^{(n)}(t_1, t_2, t_3) = & \int_0^{+\infty} dt_3 \int_0^{+\infty} dt_2 \int_0^{+\infty} dt_1 \; \mathcal{R}^{(3)}(t_1, t_2, t_3) \times \\ & \boldsymbol{\mathcal{E}}(\boldsymbol{r}, t - t_3) \boldsymbol{\mathcal{E}}(\boldsymbol{r}, t - t_3 - t_2) \boldsymbol{\mathcal{E}}(\boldsymbol{r}, t - t_3 - t_2 - t_1)\end{aligned} \tag{3.21}$$

Assuming temporally well separated laser pulses, in the so-called impulsive limit[3] (i.e the limit in which a single pulse duration is less than a single vibrational oscillation period) the third-order polarization becomes equivalent to the third order response function $\mathcal{R}^{(3)}(t_1, t_2, t_1)$ which reads:

$$\mathcal{R}^{(3)}(t_1, t_2, t_3) = \left(-\frac{i}{\hbar}\right)^3 Tr\left[\hat{\boldsymbol{\mu}}\mathbb{G}(t_3)\left[\hat{\boldsymbol{\mu}}, \mathbb{G}(t_2)\left[\hat{\boldsymbol{\mu}}, \mathbb{G}(t_1)\left[\hat{\boldsymbol{\mu}}, \hat{\rho}_0\right]\right]\right]\right] \tag{3.22}$$

The complete development of the commutators and the trace operation leads to eight independent contribution to the total signal which are called *Liouville pathways* (LP). Each one of this pathways corresponds to one of the physical processes

[3]Which means, mathematically, that the envelops of the three fields are assumed to be δ functions in time.

(i.e., ESA, GSB and SE) described earlier in this part of the thesis. However, by detecting the radiation emitted by the system in a given phase matched direction, one can selectively detect only a subgroups of *Liouville pathways*. Common choices are the so called *rephasing* direction ($\boldsymbol{k}_I = -k_1+k_2+k_3$) and *non-rephasing* direction ($\boldsymbol{k}_{II} = +k_1 - k_2 + k_3$) which become equivalent when $t_1 = 0$

3.2.1 Simulating linear and non-linear spectroscopy

Up to now, we only developed the formalism behind a given order of field-matter interaction, which translates in different spectroscopic techniques. However, by expanding Eq. 3.19 and 3.22 in an eigenstate basis of the molecular system, it is possible to visualize the quantum mechanical quantities required for the simulation of such signals. In particular, for a closed quantum system (that is, considering only the electronic degrees of freedom) the linear response function presented in Eq. 3.19 can be written as:

$$\mathcal{R}^{(1)}(t_1) = \left(-\frac{i}{\hbar}\right) \sum_e \boldsymbol{\mu}_{ge}\boldsymbol{\mu}_{eg}^{\dagger} e^{-i\omega_{eg}t_1 - \gamma_{eg}t_1} \tag{3.23}$$

where we have modeled the dephasing process of the light induced coherence phenomenologically, introducing the term γ_{eg} and we have made use of the definition of the dipole operator $\hat{\boldsymbol{\mu}} = \sum_{ij} \boldsymbol{\mu}_{ij} |i\rangle \langle j|$.
For open quantum systems (i.e., systems coupled with the environment), a microscopic origin of this dephasing is related to the coupling between electronic and nuclear degrees of freedom as we will discuss in the next part of the thesis, introducing the so called line shape function[5] $g_{eg}(t)$. For closed quantum system, at variance, the term γ_{eg} arises from the finite life time of the excited state e. The quantities of interest that are required to be computed for the simulation of linear absorption signals therefore are: (i) transition dipole moments between the ground and the excite state $|e\rangle$ (reported as μ_{ge}); (ii) the transition energy ω_{eg} between the ground and the excited states of the first excited state manifold.

In analogy we can define the GSB, SE and ESA contributions to the total spectra.

However, since now the system is able to evolve along the delay time t_2 between the *pump* and the *probe*, the expression of the signal is more complex and requires the description of the dynamics which occur during the t_2 time. For this reason, in what follows the delay time t_2 is set to 0 (i.e signals at the Franck-Condon point) while approximate ways to include dynamical effects within this formalism will be given later. The *rephasing* third-order response of the system obtained for $t_2 = 0$ than reads:

$$\mathcal{R}_{\boldsymbol{K}_I}^{(GSB)}(t_1, 0, t_3) = \left(-\frac{i}{\hbar}\right)^3 \sum_{ee'} \boldsymbol{\mu}_{eg}\boldsymbol{\mu}_{eg}\boldsymbol{\mu}_{e'g}\boldsymbol{\mu}_{e'g} e^{-i\omega_{e'g}t_3 - i\omega_{eg}t_1 - \gamma_{e'g}t_3 - \gamma_{eg}t_1} \tag{3.24}$$

$$\mathcal{R}_{\boldsymbol{K}_I}^{(SE)}(t_1, 0, t_3) = \left(-\frac{i}{\hbar}\right)^3 \sum_{ee'} \boldsymbol{\mu}_{e'g}\boldsymbol{\mu}_{eg}\boldsymbol{\mu}_{eg}\boldsymbol{\mu}_{e'g} e^{-i\omega_{e'g}t_3 - i\omega_{eg}t_1 - \gamma_{e'g}t_3 - \gamma_{eg}t_1} \tag{3.25}$$

$$\mathcal{R}_{\boldsymbol{K}_I}^{(ESA)}(t_1, 0, t_3) = \left(\frac{i}{\hbar}\right)^3 \sum_{fee'} \boldsymbol{\mu}_{eg}\boldsymbol{\mu}_{e'g}\boldsymbol{\mu}_{fe'}\boldsymbol{\mu}_{fe} e^{-i\omega_{fe}t_3 - i\omega_{eg}t_1 - \gamma_{fe}t_3 - \gamma_{eg}t_1} \tag{3.26}$$

The quantum chemical quantities required for the evaluation of these functions are: (i) transition energies and transition dipole moments between the ground state g and the first excited state manifold $\{e, e'\}$; (ii) transition energies and transition dipole moments between the first excited state manifold and the second excited state manifold $\{f\}$.

3.3 Modeling Photoelectron spectroscopy

The expressions derived until now are based on the rigorous perturbative description of the light-matter interaction that occurs during photon absorption or emission process. However, PES and XPS experiments are conceptually different from simple absorption techniques since they involve the promotion of a photoelectron to a scattering state with the consequent ionization of the molecular system. An explicit treatment of photoionization spectroscopy within the density matrix formalism is given in ref. [15], while here we discuss only the main aspects of the problem.

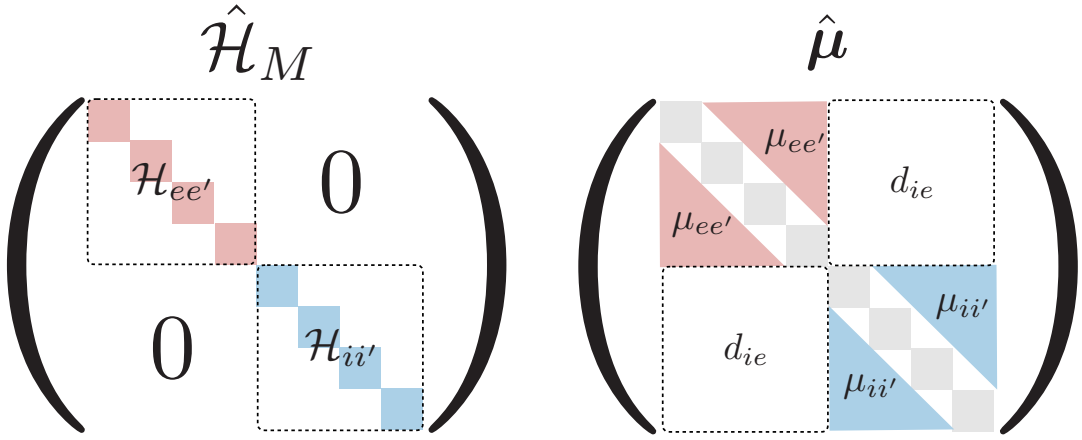

Figure 3.1: pictorical representation of the block diagonal $\hat{\mathcal{H}}_M$ operator and of the dipole operator $\hat{\boldsymbol{\mu}}$. Terms involving only neutral states are depicted in red while terms involving only cationic states are highlighted in blue. The off-diagonal terms of $\hat{\boldsymbol{\mu}}$ associated to the Dyson intensities are also showed.

In order to describe photoionization phenomena, the total Hamiltonian have to be modified in order to describe also the produced photoelectron $|p\rangle$ with a given kinetic energy k. Following the formalism proposed in Ref. [15], we use a second quantization description of the photoelectron state and a first quantization description of the bound states. In this "hybrid" formulation, the Hamiltonian can be written as:

$$\hat{\mathcal{H}} = \hat{\mathcal{H}}_M + \hat{\mathcal{H}}'(t) + \hat{\mathcal{H}}_p \tag{3.27}$$

Where $\hat{\mathcal{H}}_M$ is the molecular Hamiltonian describing both neutral and ionic state while $\hat{\mathcal{H}}_p$ is the the photoelectron Hamiltonian defined as:

$$\hat{\mathcal{H}}_p = \sum_p k \hat{c}_p^\dagger \hat{c}_p \tag{3.28}$$

Where $\hat{c}_p^\dagger(\hat{c}_p)$ are the Fermi creation(annihilation) operator for the free photoelectron.

We work in the direct product of state of continuum (photoelectron) and bound

(neutral and cationic) states which formally can be expressed as:

$$|i\rangle \cdot |p\rangle = |i, p\rangle \tag{3.29}$$

where $|i\rangle$ defines the ionic state. Within this hybrid formalism the dipole operator includes also off-diagonal terms like $\langle g| \hat{\boldsymbol{\mu}} |i, p\rangle$ which depends on the continuum state $|p\rangle$ and for this reason their evaluation becomes more cumbersome as it requires to describe the wave function of the emitted photoelectron. One can avoid the description of the continuum state noticing that, in the way we used to the define the molecular Hamiltonian $\hat{\mathcal{H}}_M$, it commutes with the photoelectron Hamiltonian $\hat{\mathcal{H}}_p$ leading to a photoelectron state which is not influenced by the potential of the bound cationic state. This correspond to a physical picture where the photoelectron is emitted with a kinetic energy large enough to rapidly escape from the molecular potential. This assumption is called *sudden approximation* and it has been typically employed for the modeling of photoelectron spectroscopy[16]. Within this approximation the aforementioned off-diagonal element $\langle g| \hat{\boldsymbol{\mu}} |i, p\rangle$ can be defined by means of so-called *Dyson intensities* (d_{gi}) as we will see in the next section[4].

In contrast with absorption spectroscopy, where the source of the signal is the n-th order polarizability, here, the source of the PES/XPS signal is the change in the number of detected photoelectrons, which can be expressed as the integrated rate of change of the number of photoelectrons occupying the continuum state:

$$\mathcal{S}(t) = \int dt \langle \dot{n}_p(t) \rangle \tag{3.30}$$

where $n_p = \hat{c}_p^\dagger \hat{c}_p$ is the occupation number of the scattering state. Noticing that n_p commutes with $\hat{\mathcal{H}}_M$ and with $\hat{\mathcal{H}}_p$ the equation of motion for $\dot{n}_p(t)$ takes the following form[12]:

$$\dot{n}_p(t) = -i \left[n_p, \mathcal{H} \right] = 2\boldsymbol{\mathcal{E}}(\boldsymbol{r}, t) \cdot \hat{\boldsymbol{\mu}} \tag{3.31}$$

[4]See Ref. [16] for a complete definition of Dyson intensities and Ref. [17] for a treatment beyond the sudden approximation.

the expectation value $\langle \dot{n}_p \rangle$ is then obtained taking the trace with the n-th order density matrix obtaining the corresponding n-th order signal $\mathcal{S}^{(n)}(t)$. In particular for the first order signal $\mathcal{S}^{(1)}(t)$ one obtains:

$$\mathcal{S}(t) = \left(-\frac{i}{\hbar}\right) \int_{-\infty}^{+\infty} d\tau_2 \int_0^{\tau_2} d\tau_1 Tr\left[\hat{\boldsymbol{\mu}} \mathbb{G}(t-\tau_2)\left[\hat{\boldsymbol{\mu}} \mathbb{G}(\tau_1), \hat{\rho}_0\right]\right] \times \boldsymbol{\mathcal{E}}(\boldsymbol{r}, t-\tau_1)\boldsymbol{\mathcal{E}}(\boldsymbol{r}, t-\tau_1-\tau_2) \tag{3.32}$$

Which can be expressed changing the time variables as:

$$\mathcal{S}(t_1) = \left(-\frac{i}{\hbar}\right) \int_0^{+\infty} dt_1 Tr\left[\hat{\boldsymbol{\mu}} \mathbb{G}(t_1)\left[\hat{\boldsymbol{\mu}}, \hat{\rho}_0\right]\right] \boldsymbol{\mathcal{E}}(\boldsymbol{r}, t-t_1) \tag{3.33}$$

This expression is now equivalent to the equation derived for the first order polarization. The same procedure can be applied to $\mathcal{S}^{(3)}(t_1, t_2, t_3)$ in order to describe TRPES and TRXPS signals. In the following we show directly the equations obtained after the expansion in the eigenstate basis:

$$\mathcal{R}^{(GSI)}(t_1, 0, t_3) = (-i)^3 \sum_{ee'} \boldsymbol{\mu}_{eg}\boldsymbol{\mu}_{eg} d_{gi} d_{gi} e^{-i(\epsilon_i - \epsilon_g + k)t_3 - i\omega_{eg}t_1 - \gamma_{gi}t_3 - \gamma_{eg}t_1} \tag{3.34}$$

$$\mathcal{R}^{(ESI)}(t_1, 0, t_3) = (-i)^3 \sum_{fee'} \boldsymbol{\mu}_{eg}\boldsymbol{\mu}_{e'g} d_{ie'} d_{ie} e^{-i(\epsilon_i - \epsilon_e + k)t_3 - i\omega_{eg}t_1 - \gamma_{ie}t_3 - \gamma_{eg}t_3} \tag{3.35}$$

Where ϵ_i, ϵ_e are respectively the energy of the cationic and of the neutral states while k is the kinec energy of the emitted photoelectron.

Part II

Modeling Molecules from gas-phase to solutions

Biological cromophores in nature shows properties which are strongly related to the environment which surrounds them. For this reason modeling the behavior of such systems requires the explicit treatment of the environment which, however, is a non trivial task. In particular, a full quantum mechanical description of the problem is typically unfeasible, due to the large size of the system (cromophore + environment), and for this reason an open quantum system formulation of the problem is typically employed. In this picture the system is described by a quantum mechanical region subjected to a perturbation induced by a classical environment. In the next part of the thesis we will introduce the quantum mechanical theory used to model the QM region of the system focusing on the computational models used to derive the QM observable of interest for the simulation of spectroscopy. We will also see how to evaluate the mutual interaction between the cromophore and the environment, introducing the main concepts of hybrid models such as QM/MM.

Finally, we will show how to couple the electronic and the nuclear degrees of freedom of the system. This coupling will be then introduced within the formalism developed in the previous part of the thesis, obtaining the methodological approach used to model the target system of this thesis, the NADH dimer.

Chapter 4

Electronic Structure Theory in a Nutshell

With "electronic structure" one typically refers to the arrangements of electrons in different energy levels in the electric field generated by static nuclei. The problem of solving the electronic structure of a given material (molecular) systems is typically tackled by solving time independent Scrhödinger equation (TISE). Different approaches to deal with TISE exits: in particular we distinguish between wave function theory and density functional theory (DFT) approaches. The first, as suggested by the name, solves the TISE through the optimization of a many-body wave function for the (many-electrons) system. Within this family is also possible to distinguish between single-reference (CC ADC) and multi-reference methods. In this thesis we will focus on the multi-reference called Compleate Active Space Self Consistent Field (CASSCF), complemented by means of second order perturbation theory (CASSCF/CASPT2). Density functional theory, at variance, is based on a different formalism, which try to compress all the information encoded in the many-body wave function within a simpler object such as the electronic density of the system. This second methodology, is cheaper compared to WF based approaches and thus is typically more suited for studying large systems. This advantage, however, come at the price of results which are dependent upon the choice of some model parameters (i.e, the exchange-correlation functional).
In the following sections the basics of the CASSCF/CASPT2 methodology will be outlined, and the flexibility of such an approach to treat states of very different nature (as, e.g., valence and core excited/ionixed states) will be shown.

4.1 Solution of the TISE

In order to find the stationary solutions of the TISE, one defines the many body electronic wave function Ψ^{el} such that:

$$\hat{\mathcal{H}}^{el}\Psi^{el} = \mathcal{E}\Psi^{el} \tag{4.1}$$

where $\hat{\mathcal{H}}^{el}$ is the electronic Hamiltonian operator of the system which can be written in the Born-Oppenheimer approximation as:

$$\hat{\mathcal{H}}^{el} = \underbrace{\sum_i \frac{1}{2}\hat{\nabla}_i^2}_{\hat{T}} + \underbrace{\sum_\alpha \sum_i \frac{Z_\alpha}{\left|\hat{\boldsymbol{R}}_\alpha - \hat{\boldsymbol{r}}_i\right|}}_{\hat{V}_{\alpha i}} + \underbrace{\sum_i \sum_{i<j} \frac{1}{\hat{r}_{ij}}}_{\hat{V}_{ij}} + \underbrace{\sum_\alpha \sum_\beta \frac{Z_\alpha Z_\beta}{\hat{R}_{\alpha\beta}}}_{\hat{V}_{\alpha\beta}} \tag{4.2}$$

Where we have labeled nuclei with Greek letters $\{\alpha, \beta, \dots\}$ and electrons with $\{i, j, \dots\}$. In this approximation the electronic wave-function is explicitly dependent on electronic coordinates, while being only parametrically dependent on the nuclear coordinates.. The same is reflected on the energy $\mathcal{E}$ of the system which can be called adiabatic energy and due to this fact the the potential part of the Hamiltonian ($\hat{V}_{\alpha\beta}$+$\hat{V}_{ij}$+$\hat{V}_{\alpha i}$) can be described by multidimensional potential energy surface $\hat{V}(\boldsymbol{\mathcal{R}})$ where $\boldsymbol{\mathcal{R}}$ represents the set of nuclear coordinates ($\{R_1, R_2, \dots, R_n\}$).

The many body wave-function has to satisfy the Pauli exclusion principle for fermions, which states that the wave-function has to change sign with respect to the swap of any possible pair of electrons:

$$\Psi^{el}(\boldsymbol{x}_1, \boldsymbol{x}_2, \dots, \boldsymbol{x}_n) = -\Psi^{el}(\boldsymbol{x}_2, \boldsymbol{x}_1, \dots, \boldsymbol{x}_n) \tag{4.3}$$

Where $\boldsymbol{x}$ is the generalized coordinate defined by the spatial and spin degrees of freedom. We can define the many body wave-function as an anti-simetrized product of one electron orthonormal spin-orbitals $\chi_i(\boldsymbol{x})$, where $\chi_i(\boldsymbol{x})$ can be factorized into a spin ($\alpha(s)$ or β(s)) and a spatial ($\varphi(\boldsymbol{r})$) component. The antisimmetrized product of such $\chi_i(\boldsymbol{x})$ is obtained trough the so-called Slater determinant (SD),

which automatically takes care of the condition4.3. The many body wave-function therefore reads:

$$\Psi^{el}(\boldsymbol{x}_1, \boldsymbol{x}_2, \cdots, \boldsymbol{x}_n) = \frac{1}{\sqrt{n!}} det \begin{bmatrix} \chi_1(\boldsymbol{x}_1) & \chi_2(\boldsymbol{x}_1) & \cdots & \chi_n(\boldsymbol{x}_1) \\ \chi_1(\boldsymbol{x}_2) & \chi_2(\boldsymbol{x}_2) & \cdots & \chi_n(\boldsymbol{x}_2) \\ \vdots & \vdots & \ddots & \vdots \\ \chi_1(\boldsymbol{x}_n) & \chi_2(\boldsymbol{x}_n) & \cdots & \chi_n(\boldsymbol{x}_n) \end{bmatrix} \tag{4.4}$$

The spatial component $\varphi_i(\boldsymbol{r})$ of the spin-orbitals are, for molecular systems, also called molecular orbitals (MOs). They are obtained as linear combination of atomic orbitals $A(\boldsymbol{r})$ (LCAO), i.e:

$$\varphi_i(\boldsymbol{r}) = \sum_j c_{ij} A_j(\boldsymbol{r}) \tag{4.5}$$

where the $A(\boldsymbol{r})$ are usually defined employing a linear combination of atom centered gaussian basis functions which have been proven to be a good compromise between the flexibility of the wave-function and the extremely fast computation of one and two-electron integrals.
The use of finite basis sets, required in actual computations, introduces an unavoidable truncation error in the computations.

4.2 Hartree-Fock solution

The Hartree-Fock (HF) solution of the TISE represent the zero*th* order approximation to the electronic structure problem. The HF approach defines the wave function as a single Slater determinant and makes use of an iterative process, called self-consistent field (SCF), to find the best set of spin-orbitals for the description of such SD in the mean field approximation[1]. This procedure employs the *variational principle*[2] where the variational degrees of freedom of the problem are the

[1]The mean field approximation describe the motion of a given electron as influenced by the mean field generated by the other electrons. In a more accurate picture, a given electron is subjected to the instantaneous potential generated by the other electrons.

[2]For which the best solution is the one which minimizes the energy of the system.

MOs coefficients c_{ij} defined in Eq. 4.5.

The HF solution can be further improved by employing Møller-Plesset perturbation theory up to different orders (MP2,MP3,etc...) to add electron correlation lost in the mean-field description. Here the HF solution is taken as the unperturbed reference and the perturbative correction is computed by the via Rayleigh-Schrödinger perturbation theory[18].

4.2.1 The correlation problem

The motion of an electron in a molecular system is intrinsically correlated to the motion of the other electrons. In particular, we distinguish two kinds of correlation: the exchange correlation and the electronic correlation. The former, which is also called spin correlation, describes the correlated motion of electrons with the same spin. The latter, which applies to electrons with the same spin, accounts for the fact that the motion of a given electron is influenced by the instantaneous positions of all the other electrons.
It is possible to show that the anti-symmetry of the Slater determinant comprises intrinsically the exchange correlation while it lacks of electron correlation. For this reason, one refers to the HF solution as an uncorrelated wave-function.

4.3 Configuration interaction

It is possible to recover the electron correlation by using the HF solution as the cornerstone upon which a correlated wave-function can be built[3]. This is obtained by relocating one or more electrons from occupied (in the HF solution) to virtual spin-orbitals, exploring all the possible electron-hole electronic configurations of the system. This corresponds to a physical picture were electron are excited from an initial occupied orbital to a final virtual orbital of the molecule. The produced configurations can thus be classified according to the number of relocated electrons

[3]A wave function allowed to span a larger portion of the complete Hilbert space in which it is defined

as singly, doubly, triply,... excited SDs, and the many body wave function is consequently defined as:

$$|\Psi^{el}\rangle = C_0 |\Psi_0\rangle + \sum_{r,a} C_a^r |\Psi_a^r\rangle + \sum_{rs,ab} C_{ab}^{rs} |\Psi_{ab}^{rs}\rangle + \cdots \tag{4.6}$$

here, $|\Psi_0\rangle$ closed shell configuration, in which all electrons reside in the optimized occupied MOs,, $|\Psi_a^r\rangle$ are all the possible 1-electron (r) 1-hole (a) configurations, $|\Psi_{ab}^{rs}\rangle$ are all the possible 2-electrons 2-holes configurations and so and so forth.
The coefficients in front of each of these terms ($C_0, C_a^r, C_{ab}^{rs}, \dots$) are called *Configuration Interaction* coefficients (CI-coefficients) and are the variational degrees of freedom of the problem. We note that, in the limit of infinite basis set and full CI (where all the possible electronic configuration are considered) such many-body wave-function gives the exact solution of the TISE. However, both infinite basis sets and full-CI approach are not feasible in practice and for this reason one always deals with solutions that truncates the expansion to some finite order. A popular example is the CI singles (CIS) solution, where the expansion is truncated at the single excitations level, and the CI singles and doubles[19] (CISD), which also includes the double excitations.

4.4 CASSCF/RASSCF approach

The Full-CI wave function of a molecular system of medium/large size involve more than billions of configurations and it is thus impossible to treat with the current technologies. However, it is not hard to realize that not all possible electronic configurations contributes equally to the wave function of the system. In fact, a given state (read wave-function) is typically defined by just a few contributions (i.e., a few non-zero CI coefficients). Given this fact, a more approximate, but still very effective methodology, called Complete Active Space Self Consistent Field (CASSCF), is typically employed in place of the Full-CI approach.
The CASSCF procedure is based on the definition of a reduced set of active MOs, called active space (AS), on which the full-CI procedure is applied. The remaining doubly occupied molecular orbital which are not placed inside the active space

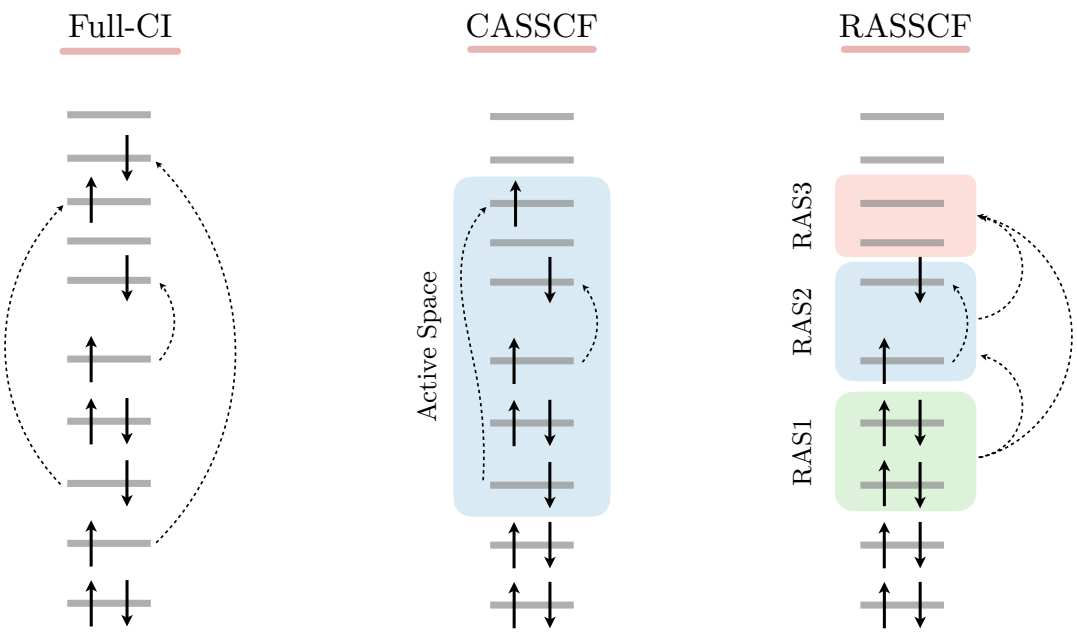

Figure 4.1: Schematic representation of Full-CI, CASSCF and RASSCF. In Full-CI all possible configurations are sampled to build the wave function. In CASSCF the same procedure is applied only to a selected set of MOs, called the Active Space (AS), therefore reducing the computational cost. A similar approach is applied in the RASSCF procedure, where the AS is partitioned in three distinct sub-spaces RAS1, RAS2, RAS3. Full-CI is performed in RAS2 while only a reduced number of holes and electrons are allowed in RAS1 and RAS3 respectively.

are called *inactive* while the virtual orbitals not included in the AS are called *secondary* orbitals. The AS definition is thus of prior importance in this method and it has to include all the MOs required to describe the problem under scrutiny with enough flexibility[4]. In order to increase the variational flexibility of the CASSCF wave function the MOs coefficients defined in equation 4.5 are optimized simultaneously to the CI-coefficients, recovering in this way effects such as orbital relaxation, which are important for the description of excited state properties.
The main drawback of this methodology is related to the factorial scaling of the

[4]e.g, describing valence excitation requires frontiers orbitals while dissociation processes require σ and σ^* orbitals corresponding to bond which is breaking.

problem with respect to the increasing size of the AS.

Further developments of the theory, focused on the reduction of the computational cost, and the enhancement of the WF flexibility, lead to the so-called Restricted Active Space Self Consistent Field (RASSCF) which represent a generalization of the CASSCF methodology. The AS is here further partitioned in three sub-spaces called RAS1, RAS2, RAS3 respectively. The active orbitals of the AS are then redistributed in these three sub-spaces and the possible configurations are built according to the following rules: a maximal number of *holes* is allowed in RAS1; full-CI is performed within RAS2;a maximal number of *electrons* are allowed in RAS3. This enables to perform a CASSCF like computation in RAS2, while still adding electron correlation with the additional flexibility provided by the restricted configuration space of RAS1 and RAS3.

Both CASSCF and RASSCF can be developed in two different fashion: *state specific* (SS-CASSCF) or *state average* (SA-CASSCF). SA-CASSCF in particular, provides a more balanced description of the wave function since it optimize a set of MOs able describe equally well the wanted number of states ensuring also their orthonormality. The ability of describing roots at equal footing is key for the simulation of transition properties, such as transition dipole moments. A schematic comparison between Full-CI, CASSCF and RASSCF is given in Fig. 4.1.

4.4.1 Computing core excited/ionized state

The higher flexibility in the definition of the wave function provided by the, RASSCF methodology, is perfectly suited for the calculation of core excited/ionized states, which poses several additional challenges.
Core excited/ionized states are created by the absorption of photons whose energy ranges from hundreds to thousands of eV. For this reason, they are preceded by an extremely large number of valence excited state, which one would prefer not to compute. Therefore, a procedure to selectively target core excited/ionized state is called for. Typically the so-called *Core Valence Separation* (CVS) is in-

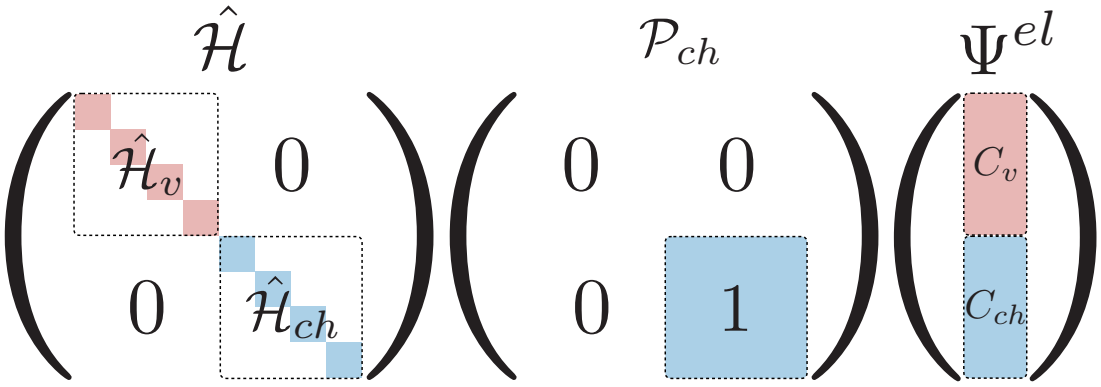

Figure 4.2: Pictorial representation of the Core-Valence separation scheme (CVS) enabled by the of the generic projection operator $\hat{\mathcal{P}}_{ch}$ (core-hole projector). In this scheme the coupling between valence and core states is neglected and thus the corresponding Hamiltonian is block-diagonal where $\hat{\mathcal{H}}_v$ and $\hat{\mathcal{H}}_{ch}$ are the blocks describing valence and core states respectively. The general projection operator $\hat{\mathcal{P}}_{ch}$ sets to zero the CI coefficients corresponding to valence excited configurations thus effectively excluding them from the description of multi-configurational wavefunction Ψ^{el}.

voked. In this approximation, valence excited and core excited states are assumed to be non interacting and they are therefore computed in separate calculations. This is practically achieved by means of particular projection operators (pictorially depicted in Fig. 4.2), that can force the exclusion of doubly occupied core orbitals from the list of configurations. An example of such projection scheme is the HEXS operator implemented in the QM package OpenMolcas[20] which sets to zero the CI-coefficients of those configurations with a maximum occupation in a given subspace, typically RAS1, where the core orbital is placed.

Since core excitation/ionization deals with core electrons, relativistic effects should also be considered[5]. In order to include these effects relativistically corrected

[5]The importance of relativistic effects for core electrons is easily understood by the following semiclassical argument: Due to the proximity of core electrons to the positive nuclei, they feel an extremely high potential which has to be balanced by equally high kinetic energy. This force the core electrons to assume very high speeds close to the relativistic limit

atomic natural orbitals basis sets are typically employed in combination with second order Douglass-Kroll-Hess (DKH) relativistic Hamiltonian[21].

4.5 CASPT2

On the top of the CASSCF/RASSCF solutions of the TISE, a further correction can be applied by means of second order perturbation theory (CASPT2/RASPT2). There are multiple way to compute such correction to the wave-function: we distinguish between *single state* (SS-CASPT2) and *multistate* (MS-CASPT2). In SS-CASPT2, each computed wave-function is taken as the zeroth order reference for the computation of the PT2 correction. In this way the perturbative correction to the energy can be evaluated separately for each state, unfortunately, obtaining non orthogonal SS-CASPT2 wave functions. In the MS-CASPT2 procedure, at variance, the PT2 correction is evaluated over a desired set of state-averaged states, and also accounts for their orthonormalization. This procedure has to be chosen when strong interaction between CASSCF states is expected. The MS-CASPT2 procedure has been developed in different flavors according to the way the reference Hamiltonian of the system is built. In this work two of these flavors are employed namely MS-CASPT2 and the extended multi state flavor of CASPT2 (XMS-CASPT2). For a more detailed review of the different CASPT2 flavors, see Ref. [22].

4.6 Computing transition probabilities

Transition probabilities between to given excited states are modeled (in the dipole approximation) by the mean of transition dipole moments, defined as:

$$\boldsymbol{\mu}_{ij} = \langle \Psi_i^{el} | \, \hat{\boldsymbol{\mu}} \, | \Psi_j^{el} \rangle \tag{4.7}$$

This is true for excitation processes but, as we have already discussed in the previous part of the thesis, this does not hold for photoionization processes where

an electron is promoted to the continuum. In this case, a strategy to account for the contiuum is required.

4.6.1 The zero*th* order description of the continuum: the Dyson orbitals

We consider a starting neutral (or charged) molecule in its ground state described by the N electron wave function $|\Psi_I^N\rangle$ which is promoted to the final ionized state described by the antisimetrized product $|\Psi_F^{N-1}\psi_p^{el}\rangle$ between the bound ionized state with $N-1$ electrons, $|\Psi_F^{N-1}\rangle$, and the wave-function of the emitted photoelectron $|\psi_p^{el}\rangle$. Within this picture the analog of the transition dipole moment defined in Eq. 4.7 reads:

$$\boldsymbol{\mu}_{IF} = \langle \Psi_F^{N-1}\psi_p^{el}| \, \hat{\boldsymbol{\mu}} \, |\Psi_I^N\rangle \tag{4.8}$$

The wave-function $|\Psi^N\rangle$ can be written in terms of Slater determinants Θ_i^N composed by single particle MOs (φ_i^k where index k runs over the set of MOs of the system) and we impose the strong orthogonality condition between the bound electrons and the emitted one ($\left\langle \psi_p^{el} \middle| \, \varphi_i^k \right\rangle = 0$), the matrix element $\boldsymbol{\mu}_{IF}$ can be expressed as:

$$\boldsymbol{\mu} = \langle \Theta_i^{N-1}\psi_p^{el}| \, \hat{\boldsymbol{\mu}} \, |\Theta_j^N\rangle = \langle \psi_p^{el}| \, \hat{\boldsymbol{\mu}} \, |\mathcal{D}_{ij}\rangle \tag{4.9}$$

where we have defined the Dyson orbital $|\mathcal{D}_{ij}\rangle$ as:

$$\mathcal{D}_{ij} = \sum_{\mathcal{P}\in\mathcal{S}_N} (-1)^p \left\langle \varphi_i^1 \, | \varphi_j^{\mathcal{P}(1)} \right\rangle \cdots \left\langle \varphi_i^{N-1} \, | \varphi_j^{\mathcal{P}(N-1)} \right\rangle \times \varphi_j^{\mathcal{P}(N)} \tag{4.10}$$

where $\mathcal{P} \in \mathcal{S}_N$ denotes all possible permutations of orbital indices with a corresponding parity p.

The Dyson orbital can be considered as an analog of the one-electron density matrix[23] and it corresponds to the wave function of the photoelectron before the ionization. The Dyson orbital for a given photoionization process is not normalized and the probability of the photoionization to occur depends on its norm (the so-called Dyson norm/Dyson intensity).

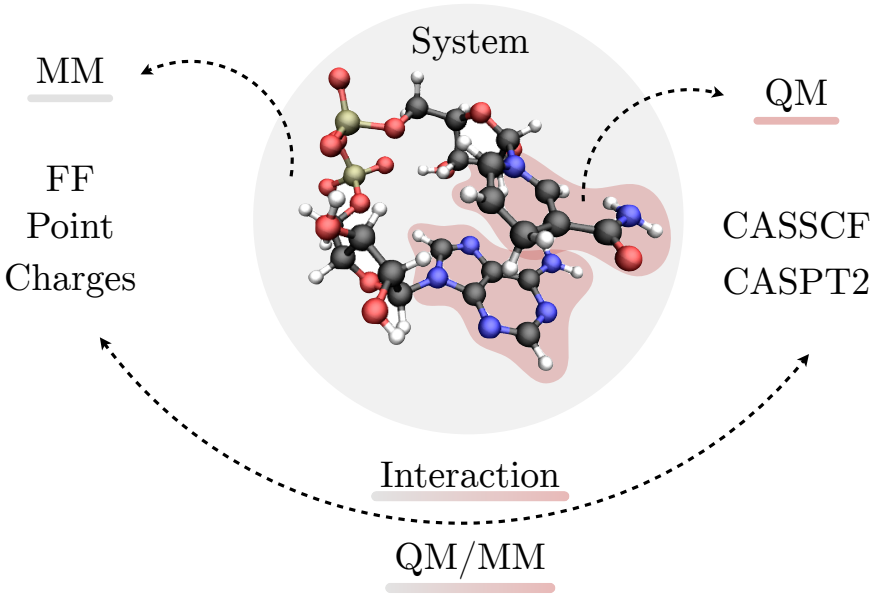

Figure 4.3: Pictorial representation of the QM/MM approach applied to the molecular target of this thesis, the NADH cromophore. The pale-red shell highlights the photo-active region of the system (that was treated here at the CASSCF/CASPT2 level of theory). Within the grey shell is depicted the MM region which is interacting with the QM part. In the *left*, FF stands for *Force Field* i.e, the sets of parameters used to describe the molecular potential in MM calculations.

4.7 Modeling of the environment: the QM/MM approach

Up to now we have discussed how to the electronic structure of isolated molecules. However, if the molecular system is embedded in a complex environment, such as a solution or a protein scaffold, the methodologies outlined until now are cannot be directly applied to treat the full molecule+environment problem. For this reason, several methodologies have been developed for the description of molecular systems dispersed in an environment. One common and cheap approach is to treat the solvent implicitly as a continuum polarizeble medium interacting with the quantum electron density of the system. This is the family of so called *Con-*

tinuum Polarizable Models (PCM) commonly applied to describe apolar aprotic solvents, which however fail in the modeling of protic solvents where directional interaction (e.g. hydrogen bonds) can occur.

For this reason since 1976 a new Hybrid methodology called QM/MM has been developed with the aim of treating the solvent explicitly. This approach is based on the partitioning of the system in sub-regions (as highlighted in Fig. 4.3) that can be treated at different levels of accuracy. In particular, the simplest scheme involve two distinct regions, one containing the photo-active system where Quantum Mechanics is applied (QM shell), and the other containing the molecules of the solvent described by the laws of Classical Mechanics (MM shell). Within this framework one of the possible approaches for the calculation of the total energy of the system (called QM/MM energy, $E_{QM/MM}$) is the so called subtractive scheme[24] which is developed as follows: (i) The electronic energy of the QM part is computed (E_{QM}); (ii) the energy of the total systems (QM+MM) is computed at the common Molecular Mechanics level ($E_{MM}(tot)$); (iii) the energy of the QM part is re-computed in a MM fashion ($E_{MM}(QM)$). The total energy is thus defined by the following equation:

$$E_{QM/MM} = E_{QM} + E_{MM}(tot) - E_{MM}(QM) \tag{4.11}$$

Within this framework the interaction between the QM and MM part of the system is encoded in the $E_{MM}(tot)$ and for this reason it is treated at classical level of theory. A more powerful approach, called electrostatic embedding enables to model more properly the electrostatic interaction between cromophore and the solvent. In this scheme the MM point charges of the solvent are directly included in the molecular Hamiltonian of the system leading to a polarization of the QM electron density. In this context, the molecular Hamiltonian defined in the Eq. 4.2 becomes:

$$\hat{\mathcal{H}} = \hat{\mathcal{H}}^{(\text{cromo})} + \sum_i \sum_m \frac{q_m}{\hat{R}_{i,m}} + \sum_\alpha \sum_m \frac{q_m}{\hat{R}_{\alpha,m}} \tag{4.12}$$

where the index m run over the MM point charges included in the Hamiltonian, defined as q_m. This approach is implemented in the computational software CO-

BRAMM[24] and it will be used in the next part of the thesis for computing QM properties of molecules in solution.

Chapter 5

Coupling to vibrations

Real systems are characterized by the presence of nuclear vibrations, which are responsible for the fluctuation of the transition energy and for energy transport process between different excited states. What we have considered so far is the electronic Hamiltonian for a fixed nuclear configuration. This is only one of the terms that describe the molecular Hamiltonian $\hat{\mathcal{H}}$, which also encodes information about the bath of vibrations coupled to the electronic degrees of freedom:

$$\hat{\mathcal{H}} = \hat{\mathcal{H}}_S + \hat{\mathcal{H}}_B + \hat{\mathcal{H}}_{SB} \tag{5.1}$$

where $\hat{\mathcal{H}}_S$ and $\hat{\mathcal{H}}_B$ are the system and bath Hamiltonian, respectively, while $\hat{\mathcal{H}}_{SB}$ is the system-bath coupling, which describes the interaction between the electronic and nuclear degrees of freedom (DOFs).
Within the models employed in this thesis, the individual terms of the total molecular Hamiltonian are given by:

$$\hat{\mathcal{H}}_S = \sum_i \epsilon_i \left|i\right\rangle \left\langle i\right| + \sum_{i \neq j} V_{ij} \left|i\right\rangle \left\langle j\right| \tag{5.2}$$

$$\hat{\mathcal{H}}_B = \sum_i \sum_{m_i} \frac{1}{2} \left(\hat{P}_{m_i}^2 + \omega_{m_i}^2 \hat{\mathcal{Q}}_{m_i}^2 \right) \tag{5.3}$$

$$\hat{\mathcal{H}}_{SB} = \sum_i \sum_{m_i} C_{m_i} \hat{\mathcal{Q}}_{m_i}^2 \left|i\right\rangle \left\langle i\right| \tag{5.4}$$

Here, $\hat{\mathcal{H}}_{SB}$ is assumed to be linear in both electronic and nuclear DOFs. Moreover, different nuclear DOFs in this framework are forced to be independent and for this reason the bath is simply described by a collection of independent harmonics modes in the nuclear phase space variables ($\hat{P}_{m_i}$ and $\hat{\mathcal{Q}}_{m_i}$) bi-linearly coupled to the electronic excitations.

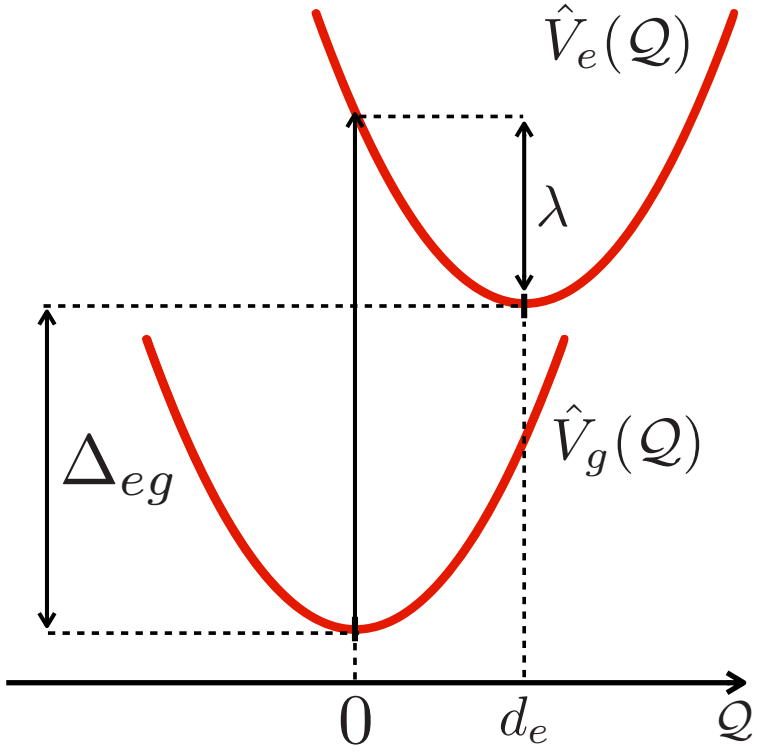

Figure 5.1: Schematic description of the Displaced Harmonic Oscillator model, with a graphical interpretation of the parameters developed in this section.

In this context, the coupling term C_{m_i} encodes the strength of the interaction between the m-th mode, with frequency ω_{m_i}, and the i-th excited state.

5.1 Spectral density function and DHO model

The properties of the system bath interaction can be summarized in the so called spectral density function $\mathcal{J}_i(\omega)$ defined as:

$$\mathcal{J}_i(\omega) = \frac{\pi}{2} \sum_m \frac{C_{m,i}^2}{\omega_m} \, \delta(\omega - \omega_m) \tag{5.5}$$

Within the framework highlighted in the previous section a simple relation between the ground state and excited state potential energy surface properties and the coupling $C_{m,i}$ can be established. In particular, we have assumed that that

both the ground and the electronic excites states are harmonic potentials along a common set of mass weighted normal mode coordinates $\mathcal{Q}_m$, characterized by with the same frequency ω_m but having different equilibrium geometries. This corresponds to a physical picture where molecules in the ground state oscillate along $\mathcal{Q}_m$ around the equilibrium position d_g (which can be set to zero without any loss of generality) while molecules in the excited state e oscillate along the same mode around a different equilibrium position d_e. This is the so called Displaced Harmonic Oscillator (DHO) model (schematically depicted in Fig. 5.1). Let us consider a two state model. The total Hamiltonian of eq. 5.1 can be rewritten as:

$$\hat{\mathcal{H}} = \hat{\mathcal{T}} + |g\rangle\,\epsilon_g\,\langle g| + \underbrace{\frac{1}{2}\sum_m \omega_m^2 \mathcal{Q}_m^2}_{\hat{V}_g} + |e\rangle\,\epsilon_e\,\langle e| + \underbrace{\frac{1}{2}\sum_m \omega_m^2\,(\mathcal{Q}_m - d_e)^2}_{\hat{V}_e} \tag{5.6}$$

where $\hat{\mathcal{T}}$ is the kinetic energy operator while $\hat{V}_g$, and $\hat{V}_e$ are respectively the ground and excited state potential energy surfaces. The energy gap between the two PES can thus be evaluated taking $\hat{V}_g$ as a reference:

$$\delta_{eg}(\mathcal{Q}_1, \cdots, \mathcal{Q}_n) = \Delta_{eg} - \sum_m^n \underbrace{\omega_m^2 d_e}_{C_{m,eg}} \mathcal{Q}_m + \frac{1}{2}\sum_m^n \underbrace{\omega_m^2 d_e^2}_{\lambda_{m,eg}} \tag{5.7}$$

Where the term Δ_{eg} is the so-called adiabatic excitation energy of the g to e transition ($\Delta_{eg} = \epsilon_e - \epsilon_g$). In the latter equation two additional terms can be also identified, in particular we call $\lambda_{m,eg}$ the so-called reorganization energy, which corresponds to the energy that the system loses during the relaxation from the Franck-Condon point to the new equilibrium position on the excited state PES. The reorganization energy can also be rewritten introducing the dimensionless (mode specific) Huang-Rhys:

$$\lambda_{m,eg} = \hbar\omega_m S_{m,eg} \tag{5.8}$$

where $S_{m,eg}$ represent the number of vibrational quanta required to obtain the reorganization energy along the mode m.

Furthermore, just by comparing Eq. 5.7 with Eq. 5.3-5.4 is possible to notice the connection between the system-bath coupling and parameters of the DHO model, identifying also a definition for the coupling strength $C_{m,eg}$ within this model.

Noticing that the reorganization energy can be also rewritten as:

$$\lambda_{m,eg} = \frac{C_{m,eg}^2}{2\omega_m^2} \tag{5.9}$$

the spectral density can be evaluated as:

$$\mathcal{J}_{eg}(\omega) = \pi \sum_m \omega_m \lambda_{m,eg} \delta(\omega - \omega_m) \tag{5.10}$$

5.2 Energy gap fluctuation auto-correlation

Within the presented model the energy gap between two different states (and thus the excitation energy) varies linearly with the modes coordinates. Following this concept we can define for a given excitation $g \to e$ the corresponding excitation energy auto-correlation function as:

$$\mathcal{C}_{eg}(t) = \langle \delta_{eg}(0)\delta_{eg}(t)\rangle = \sum_m C_m^2 \langle \mathcal{Q}_m(0)\mathcal{Q}_m(t)\rangle \tag{5.11}$$

Where $\langle\ \rangle$ indicates the equilibrium ensemble average over thermal distribution of the state of the bath. In particular this averaging process for a quantum bath of vibrations can be expressed as[5, 14]:

$$\mathcal{C}_{eg}(t) = \frac{\hbar}{2} \sum_m \left(\frac{C_m^2}{\omega_m}\right) \left[\coth\left(\frac{\beta\hbar\omega_m}{2}\right)\cos(\omega_m t) - i\sin(\omega_m t)\right] \tag{5.12}$$

Where $\beta = 1/k_B T$ comes from the equilibrium ensemble average, and the relation between the auto-correlation and the spectral density is given by[5, 14]:

$$\mathcal{J}_{eg}(\omega_m) = \frac{2}{\hbar}\tanh\left(\frac{\beta\hbar\omega_m}{2}\right) \int_0^{+\infty} dt\ \mathfrak{Re}\left[\mathcal{C}_{eg}(t)\right]\cos(\omega_m t) \tag{5.13}$$

In the next section we will finally discuss how to connect this description of the system-bath coupling with the modeling of spectroscopic signals.

5.3 Modeling transport between electronic states

Due to the interaction with the optical *pump* an excited state of the system is prepared in a non stationary state which thus evolves in time. The nuclear dynamics of the vibrational bath, as we have discussed so far, is responsible for the fluctuation of the transition energy giving thus rise to a spectral line shape which can be observed in experimental spectra. Moreover, the nuclear dynamics can couple different electronics states of the system allowing population transport to occur.

Population transports can be approximately introduced within our model at various level of sophistication. In particular, in this work we will employ a bath composed by both slow and fast fluctuations.
Fast-timescale fluctuations are typically modeled within the Markovian approximation which is fulfilled for those fluctuation that occur faster than all the other processes. During t_1 and t_3 the bath fluctuations are thus responsible for homogeneous line broadening while during t_2 they cause population transport. In the limit of decoupled populations and coherence (secular approximation) the population relaxation can be described by a Pauli master equation:

$$\frac{\partial \hat{\rho}_{ee}(t)}{\partial t} = -\sum_{e'} \mathcal{K}_{ee,e'e'} \hat{\rho}_{e'e'}(t) \tag{5.14}$$

Here $\mathcal{K}_{ee,e'e'}$ is the rate matrix element of $\hat{\mathcal{K}}$ encoding for the transport rate from state e to state e'. In this framework this term is assumed to be independent of the fluctuation of the slow modes. The solution of this differential equation is formally given by:

$$\hat{\rho}_{e'e'}(t) = \sum_{e} \mathcal{G}_{e'e',ee} \hat{\rho}_{ee}(0) \tag{5.15}$$

Where $\mathcal{G}_{e'e',ee}$ are the elements of the $\hat{\mathcal{G}}$ matrix which is also called population

Green's function. The $\mathcal{G}_{e'e',ee}$ elements describe the time dependent probability of a bath assisted transition between e and e'.
The slow-timescale modes, at variance, are only responsible for spectral diffusion during the three intervals t_1, t_2 and t_3.

The secular approximation allows to further partition the non linear response in population ($e = e'$) and coherence ($e \neq e'$) contribution to the total signal. In particular the Population contributions reads:

$$\mathcal{R}^{(GSB)}_{\boldsymbol{K}_I,(P)}(t_1,t_2,t_3) = \left(-\frac{i}{\hbar}\right)^3 \sum_{ee'} \mu_{eg}\mu_{eg}\mu_{e'g}\mu_{e'g} \times \\ \times\, e^{-i\omega_{e'g}t_3 - i\omega_{eg}t_1 + \varphi^{GSB,(P)}_{ege'}(0,t_1,t_1+t_2+t_3,t_1+t_2)} \tag{5.16}$$

$$\mathcal{R}^{(SE)}_{\boldsymbol{K}_I,(P)}(t_1,t_2,t_3) = \left(-\frac{i}{\hbar}\right)^3 \sum_{ee'} \mu_{eg}\mu_{eg}\mu_{e'g}\mu_{e'g}\mathcal{G}_{e'e',ee}(t_2) \times \\ \times\, e^{-i\omega_{e'g}t_3 - i\omega_{eg}t_1 + \varphi^{SE,(P)}_{ege'}(0,t_1+t_2,t_1+t_2+t_3,t_1)} \tag{5.17}$$

$$\mathcal{R}^{(ESA)}_{\boldsymbol{K}_I,(P)}(t_1,t_2,t_3) = \left(-\frac{i}{\hbar}\right)^3 \sum_{fee'} \mu_{eg}\mu_{e'g}\mu_{fe'}\mu_{fe}\mathcal{G}_{e'e',ee}(t_2) \times \\ \times\, e^{-i\omega_{fe}t_3 - i\omega_{eg}t_1 + \varphi^{ESA,(P)}_{fe'e}(t_1,t_1+t_2,t_1+t_2+t_3,0)} \tag{5.18}$$

While the coherence contributions reads:

$$\mathcal{R}^{(SE)}_{\boldsymbol{K}_I,(C)}(t_1,t_2,t_3) = \left(-\frac{i}{\hbar}\right)^3 \sum_{e\neq e'} \mu_{eg}\mu_{eg}\mu_{e'g}\mu_{e'g} \times \\ \times\, e^{-i\omega_{e'g}t_3 - i\omega_{e'e}t_2 - i\omega_{eg}t_1 + \varphi^{SE,(C)}_{ege'}(0,t_1+t_2,t_1+t_2+t_3,t_1)} \tag{5.19}$$

$$\mathcal{R}^{(ESA)}_{\boldsymbol{K}_I,(C)}(t_1,t_2,t_3) = \left(-\frac{i}{\hbar}\right)^3 \sum_{e\neq e'}\sum_{f} \mu_{eg}\mu_{e'g}\mu_{fe'}\mu_{fe} \times \\ \times\, e^{-i\omega_{fe}t_3 - i\omega_{e'e}t_2 - i\omega_{eg}t_1 + \varphi^{ESA,(C)}_{fe'e}(t_1,t_1+t_2,t_1+t_2+t_3,0)} \tag{5.20}$$

Since only one ground state is present, no coherence contribution are observed for the GS. In this series of equations the terms labeled as φ are the *phase-functions*

which describe the coupling to the vibrational bath and they are given by the following equations:

$$\varphi^{GSB,(P)}_{ege'}(0,t_1,t_1+t_2+t_3,t_1+t_2) = \delta_{ee'}\phi^{(C)}_{ege'}(0,t_1,t_1+t_2+t_3,t_1+t_2) \quad (5.21)$$

$$\varphi^{SE,(P)}_{ege'}(0,t_1+t_2,t_1+t_2+t_3,t_1) = \delta_{ee'}\phi^{(C)}_{ege'}(0,t_1,t_1+t_2+t_3,t_1+t_2) + \xi_{ee'}\phi^{(I)}_{e'ge'e}(t_1,t_2,t_3) \quad (5.22)$$

$$\varphi^{ESA,(P)}_{fe'e}(t_1,t_1+t_2,t_1+t_2+t_3,0) = \delta_{ee'}\phi^{(C)}_{efe}(t_1,t_1+t_2,t_1+t_2+t_3,0) + \xi_{ee'}\phi^{(I)}_{fe'e'e}(t_1,t_2,t_3) \quad (5.23)$$

$$\varphi^{SE,(C)}_{ege'}(0,t_1+t_2,t_1+t_2+t_3,t_1) = \phi^{(C)}_{e'ge}(0,t_1,t_1+t_2+t_3,t_1+t_2)$$

$$\varphi^{ESA,(C)}_{fe'e}(t_1,t_1+t_2,t_1+t_2+t_3,0) = \phi^{(C)}_{e'fe}(t_1,t_1+t_2,t_1+t_2+t_3,0) \quad (5.24)$$

Where $\xi_{ee'} = 1 - \delta_{ee'}$. The phase functions of the population contribution to ESA and SE contains both a coherent ($\phi^{(C)}$) and an incoherent ($\phi^{(I)}$) contribution, the former describing population-conserving Louville-pathways (path in which the transport is not involved) and the latter population-transfer pathways in which the Markovian approximation is applied to the fast modes. The terms labeled as ϕ are the four-point line shape functions[5] which are obtained via the the second-order Cumulant expansion of Gaussian Fluctuations[14] (CGF). This therms can be expressed as a combination of two-point line shape functions defined as[5]:

$$g_{ij}(t_1) = -\frac{1}{2\pi}\int_0^{+\infty} d\omega\ \frac{\mathcal{J}_{ij}(\omega)}{\omega^2}\left[\coth\left(\frac{\beta\omega}{2}\right)(1-\cos(\omega t)) + i\left(\sin(\omega t) - \omega t\right)\right] \quad (5.25)$$

where i and j are used to label two different electronic states.

We have finally derived all the main equations employed in the simulation of steady state and time-resolved spectroscopy. In the following, and last section of this chapter, we will introduce the computational workflow used to simulate spectra in practice.

5.4 Computational Workflow

Until now we have derived an elegant and compact theory for the modeling of spectroscopic signals. To be employed in spectroscopy simulation, this theoretical framework requires as the computation of some quantities: (i) the transition energies between the states; (ii) the transition dipole moments/Dyson norm between the states interrogated by the lasers; (iii) the spectral density for each state included in the model. In what follows a general computational workflow for the evaluation of these quantities is outlined:

1. MP2 optimization on the molecular ground state.
2. Frequency and normal modes calculation at the MP2 level is preformed since these quantities are required for the evaluation of the spectral density.
3. Electronic structure calculations are required for the simulation of spectroscopic signal. Different kind of spectroscopies require slightly different simulation protocols:
    - UV-VIS: linear and PP signals can be obtained by means of CASSCF/CASPT2 calculations. In general, a single state average calculation is enough for the description of the valence excited states in both the e and in the f manifold.
    - EUV: (TR-)PES requires the calculation of valence ionized states which has to be computed in separate state average calculations with respect to valence excited states. For this reason a first CASSCF/CASPT2 computation is run in order to obtain the ground (which is the only state required for the PES) and valence excited states (required for TR-PES). Subsequently, valence ionized states are computed in a different CASSCF/CASPT2 calculation by considering the cationic species and forcing the spin multiplicity to be 2.
    - X-Ray: (TR-)NEXAFS and (TR-)XPS similarly to (TR-)PES require two separate calculations for core and valence states. Moreover, as

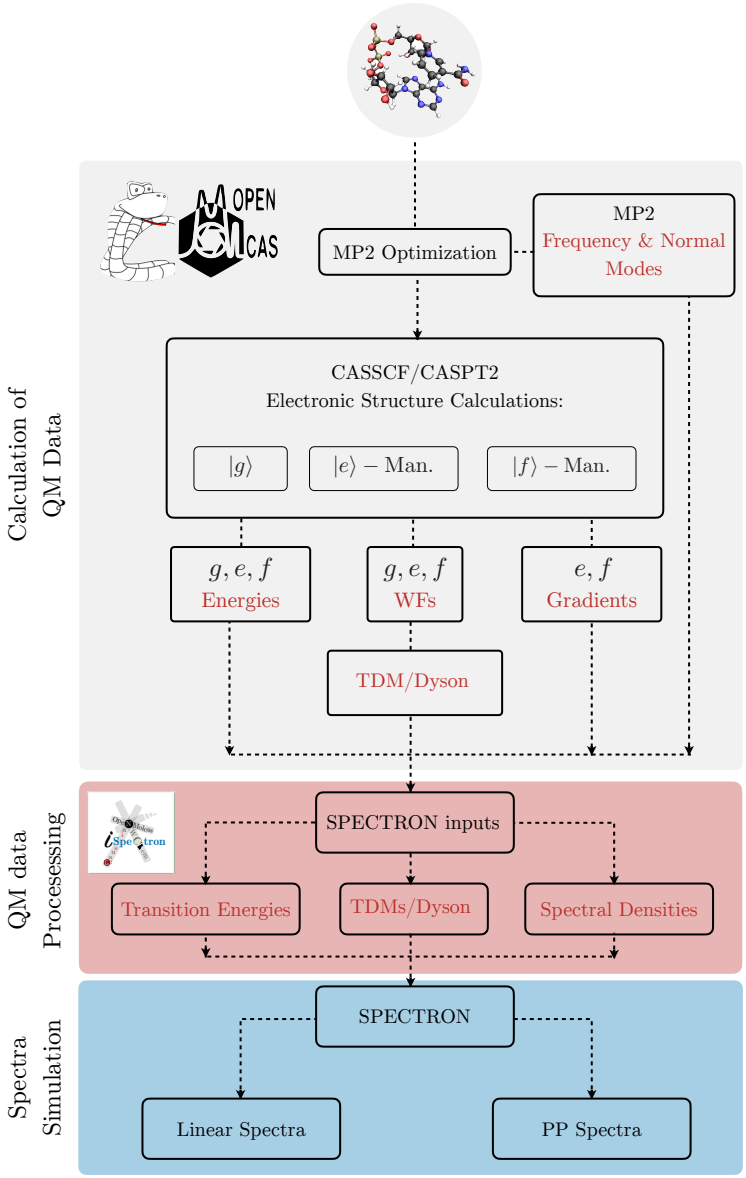

Figure 5.2: Flowchart of the computational workflow used to simulated linear and PP spectroscopy in different spectral windows. The key steps of the protocol are outlined: calculation of QM data of interest; their processing trough the software iSPECTRON and simulation of the signals with SPECTRON.

introduced in the previous chapter, they also require the RASSCF approach to be coupled with a specific projection scheme able to specifi-

cally target core-hole configurations. (TR-)XPS requires the same procedure of (TR-)PES complemented with the above mentioned projection scheme (to force the ionization to occur in the core orbital)
Ground and valence excited states have also to be re-computed at the same level of theory (RASSCF/RASPT2) in order to model transition properties such as transition energy and transition dipole moments.

In addition, the same active space structure (number of orbitals and electrons, allowed electrons and holes) have to be selected for those spectroscopic techniques which requires separate electronic structure calculations.

4. Transition dipole moments (TDMs) or Dyson norms calculation are then performed.

5. Excited states gradients are computed at CASSCF/CASPT2 or RASSCF/RASPT2 level by means of numerical differentiation in order to obtain the vibronic coupling strength (C_m) defined in Eq. 5.7. The connection between coupling strengths and gradients is made apparent realizing that:

$$\begin{aligned}\boldsymbol{\nabla}(\boldsymbol{\mathcal{Q}})\,\big|_{\boldsymbol{d}_g}\,\hat{V}_e(\boldsymbol{\mathcal{Q}}) &= \boldsymbol{\nabla}(\boldsymbol{\mathcal{Q}})\,\big|_{\boldsymbol{d}_g}\left[\sum_m \frac{1}{2}\omega_m\,(\boldsymbol{\mathcal{Q}}_m - \boldsymbol{d}_m^e)^2\right] \\ &= -\sum_m \omega_m\,(\boldsymbol{d}_m^e - \boldsymbol{d}_m^g) = -\boldsymbol{C}_m \end{aligned} \tag{5.26}$$

This computational methodology is called *vertical gradient approach.*

6. The QM data of interest are processed with the code iSPECTRON[25] in order to prepare the input for the SPECTRON package which allows for spectroscopy simulation within the framework explained above. In particular, iSPECTRON is used: to process frequency, normal modes and vertical gradients to obtain the spectral density functions. Until now we only present the *intra-molecular* part of the spectral density which encodes the information about the coupling between the system and the *intra-molecular* bath of vibration. However, for systems in solution, the coupling with *inter-molecular*

vibrations should be also considered. In particular, the *inter-molecular* part of the spectral density $\mathcal{J}^{inter}(\omega)$ usually contains a quasi-continuum of low frequency contributions and, for this reason, it is often substituted by analytical model functions. In this work the model employed is the so-called Overdamped Brownian Oscillator[26] (OBO) defined by the following spectral density:

$$\mathcal{J}^{inter}(\omega) = 2\lambda \frac{\omega/\gamma}{(\omega/\gamma)^2 + 1} \tag{5.27}$$

where λ is the reorganization energy and γ is a damping constant.

This protocol (also summarized in Fig. 5.2) can be applied for the simulation of spectroscopic signals for both isolated or solvated molecules. In this work, electronic structure calculations performed on isolated molecules are run with the quantum chemistry package OpenMolcas[27] while calculation on solvated systems are run with the software COBRAMM[24].

Part III

Results

Here we make use of the concepts developed in previous parts of the thesis and we study of a real system, namely, the Nicotimanide Adeninine Dinucleotide dimer in its reduced form (NADH).

The NADH system shows an intriguing photo-chemistry. Let us consider a scenario where this dimer, dissolved in water solution, is illuminated with a light around 260 nm (where it is known to absorb). The interaction with the pulse promotes the system on the L_A state of adenine, initiating an excited state relaxation dynamics on in that. The fluorecence of the system can be detected, and it is expected to resemble the emission spectrum of pure adenine. But, the recorded fluorescence spectrum can be actually attributed to the other moiety of the system, the reduced nicotinamide. This point towards an energy transfer process between the adenine and the nicotinamide moieties, as it was rationalized by Weber et. al.[28].
After these first observations several experiments have been carried out with the aim to understand the mechanism behind this process[28, 29]. However due to the complexity of the system a clear understanding of the photo-induced process is still missing and a time-resolved technique capable to resolve such ET process is called for.

In this part of the thesis what is already known about the NADH dimer and its ET process will be briefly introduced. Than the (already available) *pump-probe* experiments in the UV-VIS window will be discussed, carefully comparing them with our first-principles spectroscopy simulations, highlighting the limitations of such experimental technique. A detailed comparison of TR-PES, TR-NEXAFS and TR-XPS is then performed, aimed at identifying the time-resolved spectroscopy best suited to study the ET process in NADH.

Chapter 6

Theoretical Investigation of the Energy Transfer Process in NADH

6.1 Introduction

Since the first observation by Weber[28], the energy transfer process in the NADH has been extensively studied for almost 60 years. It has been observed that the rate of this ET process is influenced by the distance and the orientation of the two moieties, which is in turn dictated by temperature, pH and solvent polarity. Moreover, it has been indirectly proven by recent experimental studies[30] that this process occurs in less than 100 femtoseconds in water.

In their recent experimental work[30], Heiner and coworkers classify this process as a Förster type energy transfer. Förster theory[14] is typically invoked when the relevant electronic states of the interacting cromophores are only weekly coupled and when the donor fluorecence overlaps with absorbance of the acceptor. This corresponds to a physical picture where the excited state of the donor D (i.e the L_A state of the adenine moiety) relaxes toward its energy minimum and, from this position, a resonant energy transfer takes place leading to a depletion of the donor population with a consequent increasing in the population of the acceptor (A). The weak coupling conditions appears to be fulfilled in the NADH dimer as its linear absorption spectrum appears as a simple sum of the spectra of the two individual monomers (see 6.1-(a)). However, the ultrafast timescale proposed by Heiner et al., much faster than any vibrational relaxation scale, contradicts the other assumption of a Förster type energy transfer. In fact, in this early time after the optical excitation the system is in a non-equilibrium regime and the wave

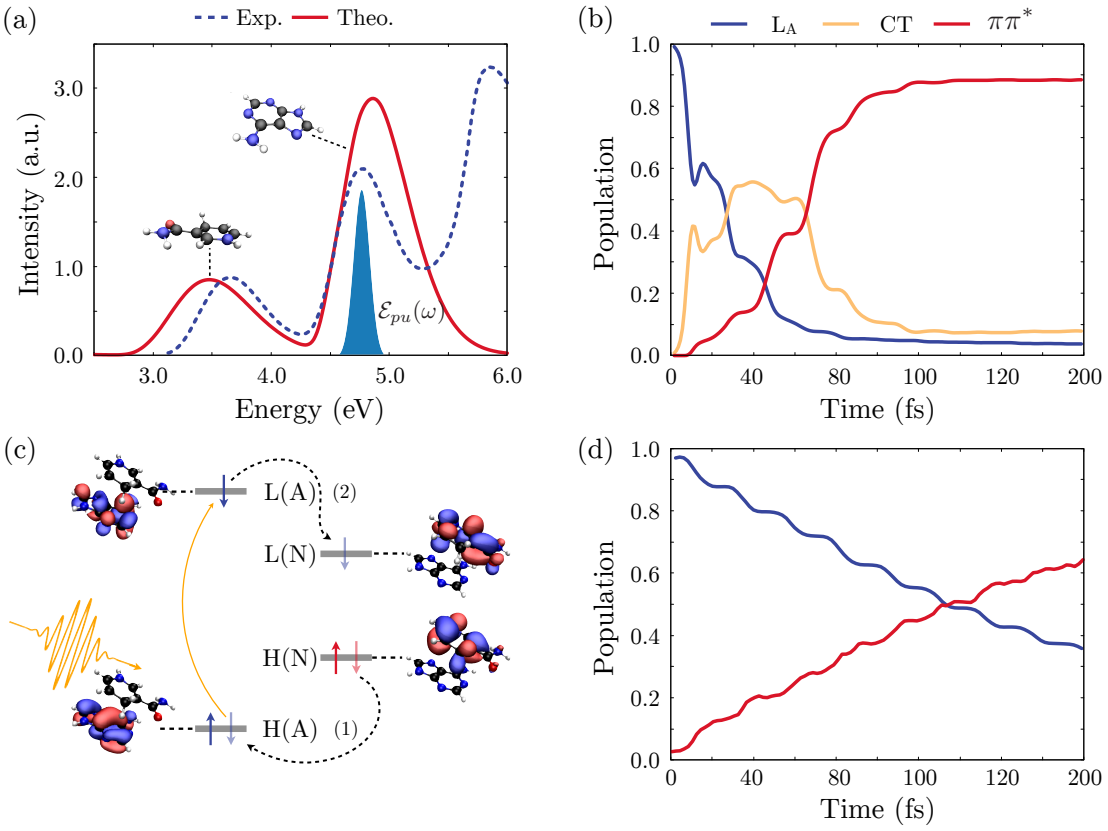

Figure 6.1: Summary of the already known properties of NADH. In (a) the linear Absorption spectra of NADH recorded in phosphate buffer solution (PBS) is depicted with a blue dotted line while the theoretical simulation is highlighted in red. A rigid shift towards the blue of 0.4 eV is applied to theoretical result in order to align it with the experiment. The pump pulse enveloped $\mathcal{E}_{pu}(\omega)$ applied for the measurement of *pump-probe* spectroscopy is also schematically depicted by the pale-blue Gaussian. (b) shows the population dynamics obtained at the MCTDH level when the CT state is considered in the model while (d) shows the population dynamics obtained employing the same level of theory but excluding the CT state from the model. Finally, (c) pictorially depict the energy transfer mechanism as two photo-redox process.

packet prepared by the light pulse is still evolving coherently.

For this reason a more in depth quantum-mechanical study is required to elucidates the process. To this aim, an MCTDH quantum dynamics simulations employing a linear vibronic coupling model[31] (LVC) was run to uncover the coherent nature of the process. These calculations showed how a coherent non-adiabatic description of this mechanism is more suited for the modeling of the energy transfer process which is accelerated by a charge transfer state between the two moieties as reported in figure 6.1-(b,d). In this context, a direct mechanism where the coupling between the donor and acceptor moieties is governed by the Dexter interaction[32], can be also considered as opposite to the CT-mediated mechanism. The Dexter mechanism involves the simultaneous exchange of two electrons which is $H(A)^{(1)}H(N)^{(2)}L(A)^{(1)}$ to $H(A)^{(2)}H(N)^{(1)}L(N)^{(1)}$ (where $H(A)$ and $L(A)$ are the HOMO and LUMO orbitals of the the adenine moiety whereas $H(N)$ and $L(N)$ are the corresponding orbitals of the nicotineamide moiety). The CT mechanism is a two-step sequential mechanism. In the first step a $H(N) \rightarrow H(A)$ or a $L(A) \rightarrow L(N)$ one electron transfer leads to the formation of a CT with configuration $H(A)^{(2)}H(N)^{(1)}L(A)^{(1)}$ or $H(A)^{(1)}H(N)^{(2)}L(N)^{(1)}$, respectively. In the subsequent step the $\pi\pi^*$ state of nicotinamide is formed by a second one electron transfer restoring neutrality. The preference for one of these paths is dictated by the energy of the CT state populated in the first step. A schematic representation of this mechanism is given in figure 6.1-(c).
Both the Direct and the CT-mediated mechanism depend on the $\langle H(N)|\, H(A)\rangle$ and $\langle L(N)|\, L(A)\rangle$ overlaps but the Dexter mechanism depends on the distance of the electronic densities of the two moieties while the CT-mediated channel depends on the energetic proximity between the intermediate CT state and final and initial states.

A clear experimental evidence which supports this theory is still missing. In this chapter the *pump-probe* UV-VIS spectra for this system is simulated by means of the protocol outlined in the last parts of the thesis. The mechanism proposed by the quantum-dynamics calculations is assumed for the spectroscopy simulation. A comparison with current existing experimental spectra is also performed with the aim of understand why a clear evidence of this mechanism is still missing.

6.2 Theoretical approach

Due to structural flexibility of NADH, a variety of conformers can be found in solution. For this reason a sampling of the conformational space is required. Different conformations are here sampled using replica exchange molecular dynamics in the framework usually employed for nucleosides as reported in Ref.[33]. The sampled conformers are subsequently analyzed by means of Cluster Analysis obtaining the most populated folded conformations. These conformers shows a pronounced heterogeneity in the relative orientation of the two moieties and they are thus characterized by different inter-base distance and different mutual stacking interactions. Moreover, the folded conformer represent just a sub-population of the total molecules which can also exist in a more populated unfolded conformation (75:25 unfolded/folded ratio determined by NMR studies[34]). The spectroscopic simulations are performed taking as reference the most representative unfolded and folded conformations. On the top of the selected structures a further electrostatic embedding QM/MM optimization in water is performed using the QM/MM package COBRAMM[24].

6.2.1 QM/MM set-up

The QM/MM setup comprises a spherical droplet of 500 water molecules which surround the NADH dimer. The full system is partitioned in three distinct subshells called low/medium/high layer respectively: (i) The high layer consists of the two bases which are optimized quantum-mechanically at the MP2 level of theory employing 6-31G* basis-set; (ii) The medium layer is composed by the nearest hydrogen-bonded water molecules and by the flexible backbone of the system and it is optimized at MM level; (iii) The low layer consists only of water molecules, treated at MM level, and it is kept frozen during the QM/MM optimization[1]. The same partitioning is also applied to the frequency and normal modes calculation.

[1] the solvent droplet is previously equilibrated by means of molecular dynamics.

6.2.2 Multiconfigurational calculations

In order to simulate the *pump-probe* spectroscopy of this system electronic structure calculations are required to obtain the transition energies and transition dipole moments between different excited states. Energy gradients of the valence excited states are also required by the DHO model. These quantities are computed for the folded and unfolded conformation employing the CASSCF/CASPT2 methodology slightly adapted in the following way:

In the unfolded conformation, due to the large distance between the to moieties, only Förster resonant energy transfer can occur. This aforementioned processes takes place in a different time scale compared to what is observed in the quantum dynamics simulations and therefore it is neglected in this study. The *pump* pulse employed in experimental investigation is centered around 4.75 eV and it is sharp enough to prepare selectively the L_A state of adenine (as shown schematically in figure 6.1-(a)), and thus only excited states localized on the adenine moiety can be included in the model for the simulation of spectroscopy. In particular, the deactivation pathways followed by the unfolded conformation is assumed to be an internal conversion from the L_A to the ground state as reported in previous theoretical[35, 36] and experimental[37] investigations on water solvated adenosine.
An active space only consisting of MOs localized on adenine is construct. In particular, 4 doubly occupied π orbitals and 4 virtual π^* orbitals are included in the AS and the computation of the valence excited states is achieved by means of state average CASSCF(8,8) including 20 roots in the excited state manifold. Single state CASPT2 correction was performed on the top of the CASSCF solution. Finally, excited state gradients are computed by means of analytical differentiation at the CASSCF level.
For these calculation the nicotinamide moiety, which has not be considered so far, was also placed with the QM layer but its frontier orbitals were kept outside from the AS.

The folded state is responsible for the energy transfer process and for this rea-

son, both the excited states of adenine and of nicotinamide have to be included in the model. Due to the large size of the system the calculation of the higher lying state (i.e., the states involved in the $|f\rangle$-manifold) was not achieved in single calculation but rather they were obtained running separate calculations on the two bases, this is also motivated by the weak exciton coupling which indicates a weak wave-function mixing. In particular for the adenine moiety the same aforementioned set-up was used while, to excite states localized over nicotinamide, an AS concerning of 3 doubly occupied π orbitals and 2 virtual π^* orbitals has been employed. The excited states computations were run in a state average fashion including 5 roots in the excited state manifold. Extended multistate CASPT2 (XMS-CASPT2) correction was applied on the top of the CASSCF solution. This procedure has been chosen since a large coupling was found between the excited states of nicotinamide.
In order to describe the CT state and its ESA contributions a calculation of delocalized states (i.e., excited states involving both chromophores) was also performed. The active space for this calculation was constructed by including 4 doubly occupied (π) and 4 virtual (π^*) orbitals localized upon adenine and 2 doubly occupied (π) and 2 virtual (π^*) orbitals localized upon nicotinamide. The excited states calculation was performed in a state average CASSCF procedure over 15 states followed by a SS-CASPT2 correction. Energy gradients were obtained by numerical differentiation at the CASSCF.

For each of the aforementioned computations the transition dipole moments were also computed by means of a RAS state interaction procedure (RASSI). The calculation of delocalized states is used only to evaluate the transition dipole moments between the CT and the higher lying states which are responsible for the ESA contribution arising from the population in such state.
For the simulation of the total spectrum the signals produced by the folded and by the unfolded conformations have to be combined and weighted according to their statistical occurrence. In particular not all the sampled folded conformations are able to undergo energy transfer. For this reason only the 50% of the folded

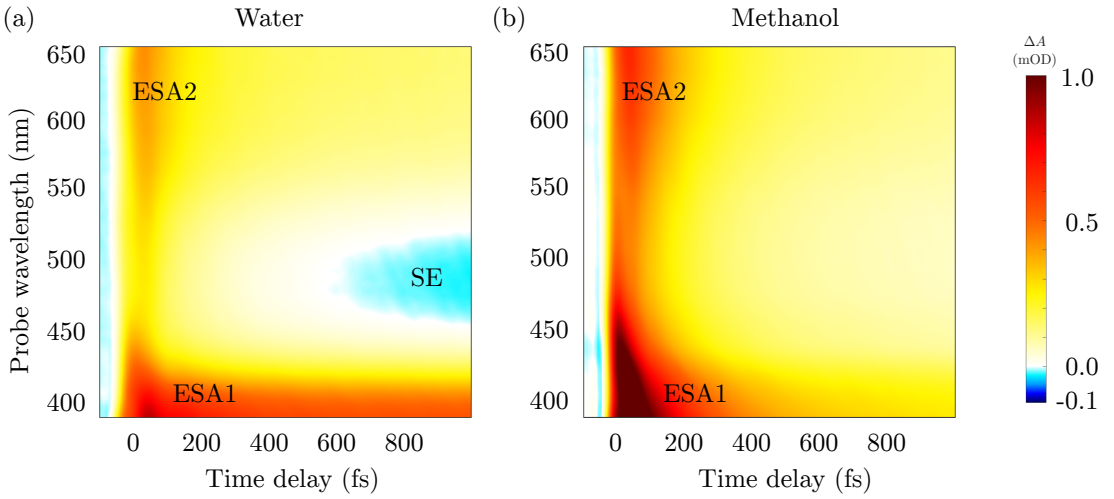

Figure 6.2: experimental results obtained for NADH in both water (a) and methanol (b) recorded employing a magic angle polarization between the two pulses. Note the different behaviour of the dimer in two solvents in particular the long living ESA1 signal centered at 400 nm observed in (a) which is missing in (b) and the build up of the stimulated emission of nicotinamide around 500 nm. The intensity is reported as differential optical density ΔA in mOD units.

molecules in the folded state is assumed to be involved in the energy transfer process (which means only 12.5% of the full population) while the entire unfolded population is assumed to undergo internal conversion towards the GS.
The results of the electronic structure calculation have also shown that the lower energy CT state, and thus the one involved in the ET, is characterized by the $H(A)^{(1)}H(N)^{(2)}L(A)^{(0)}L(N)^{(1)}$ electronic configuration (characteristic of the first path discussed in above). Only this CT state was included in the model.

The final theoretical spectrum is further convoluted over time applying a Gaussian convolution function with a standard deviation of 20 fs in order to approximately account for the finite pulse duration of the experimental set-up.

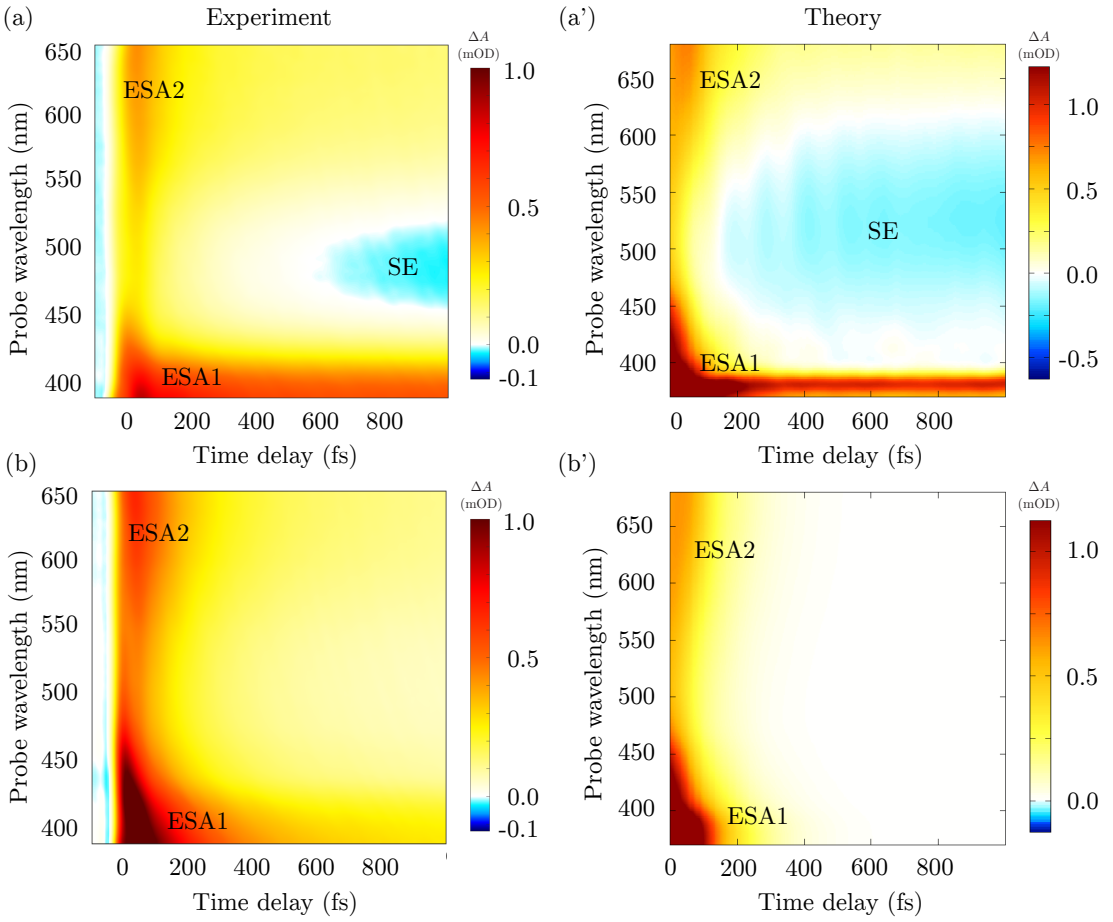

Figure 6.3: Comparison between experimental and theoretical results obtained for a magic angle polarization of the two pulses. Section (a) and (a') highlight the comparison between the experimental spectrum recorded in water with the corresponding simulation. Section (b) and (b') display the comparison between the experiment performed in methanol with the computed spectra for the unfolded conformation of NADH in water. The intensity of the signals is reported as differential optical density ΔA in mOD units.

6.3 Experimental and theoretical results

Experimental results for the NADH dimer in water and methanol solution are presented in figure 6.2-(a) and 6.2-(b) respectively[2]. The two spectra presented here

[2]The experimental data reported here comes form unpublished data by Prof. Giulio Cerullo's group.

agree with the previous results reported in Ref. [30] which are however recorded with a lower time resolution. The PP spectrum recorded in water is characterized by the presence of a strong ESA contribution around 400 nm (ESA1) which shows a decay of its intensity until the reaching of a constant value after 200 fs. Similar behaviour is shown by the ESA contribution around 600 nm (ESA2). Around 475 nm the spectrum recorded in water shows also a SE contribution which can be addressed as the SE of nicotinamide since it resemble its fluorecence spectra.

The spectrum recorded in methanol, at variance, shows a different scenario. The long living signal labeled as ESA1 in figure 6.2-(a) here is replaced by a shorter living signal which decay, almost completely, around 300 fs. Moreover, the spectrum recorded in methanol (6.2-(b)) displays a progressive blue shift of the ESA1 signal which can be related to the ballistic motion of the wave-packet towards the L_A/GS conical intersection. The ESA2 signal, on the other hand, is still showing a similar behaviour in the two different solvents while the buildup of the SE of nicotinamide is absent in the spectrum recorded in methanol. Since the long living ESA1 and the SE signals are quenched together in the experiment recorded in methanol one can conclude that they are arising from the same excited state which is, in particular, the $\pi\pi^*$ collector state of nicotinamide. By looking carefully to the spectrum recorded in methanol at around 400 nm some low intense long living signal is still observed, suggesting that only a very small percentage of the system is undergoing the ET process.

In order to understand the different behaviours displayed by the dimer in the two solvents theoretical simulations are invoked and the results of the comparison with experiments is reported in figure 6.3. Theoretical spectrum (Fig. 6.3-(a')) is qualitatively in agreement with the experimental results. In the computed PP map the $\pi\pi^*$ SE emission appear to be more intense, and more broad, compared to its experimental counterpart. This leads to the partial covering of the ESA2 signal which appear to be red-shifted compared to experiments. ESA1 signal, at variance, appear to be more sharp in the simulation probably due to the low amount of static disorder included in the model which may increase the broadening of the computed signals. The buildup of the stimulated emission in the theoretical and

experimental spectra seems to occur at different times. however, by analyzing the experimental results a correlation between the SE and the long living part of ESA1 can be established since they are produced by the same state. The ESA1 signal, as already discussed, displays a decay until a constant intensity is reached at 200 fs. At early times this signal arises form the L_A state which is decaying in this time scale. After 200 fs the ESA1 signal is then associated only to the long living ESA of nicotinamide and for this reason also the SE signal should be observed in the same time-scale. The delay in the buildup of the stimulated emission have thus to be explained as due to the overlap with some background signals which disappear around 600 fs. In the theoretical map the same delay is not observed again due to the higher intensity displayed by the computed SE.
Figures 6.3-(b)&(b'), at variance, highlight the comparison between the experimental spectrum recorded in methanol and the PP map computed assuming 100% of unfolded dimer. In this case the agreement is almost quantitative suggesting that the population of the folded conformation in methanol is negligible compared to the unfolded state. The computed PP map, however, is not completely reproducing the blue shift displayed by the ESA1 signal discussed above. The DHO model, in fact, is not able to simulate the ballistic motion of a wave-packets toward conical intersections.

6.4 CT state sensitivity

Until now we have discussed about the signals recorded in the UV-VIS experimental PP map and how they can be assigned to the energy transfer process. However, no clear signatures of the charge transfer state have been observed so far. In the following the individual contributions, of the states involved in this process, which give rise to the total spectrum will be disentangled trying to understand way a signature of the CT state is missing.
Spectroscopic simulation including in the model only one valence state at time are performed and the corresponding results are highlighted in figure 6.4. At a first glance, one can note the presence of a characteristic ESA signal associated to the

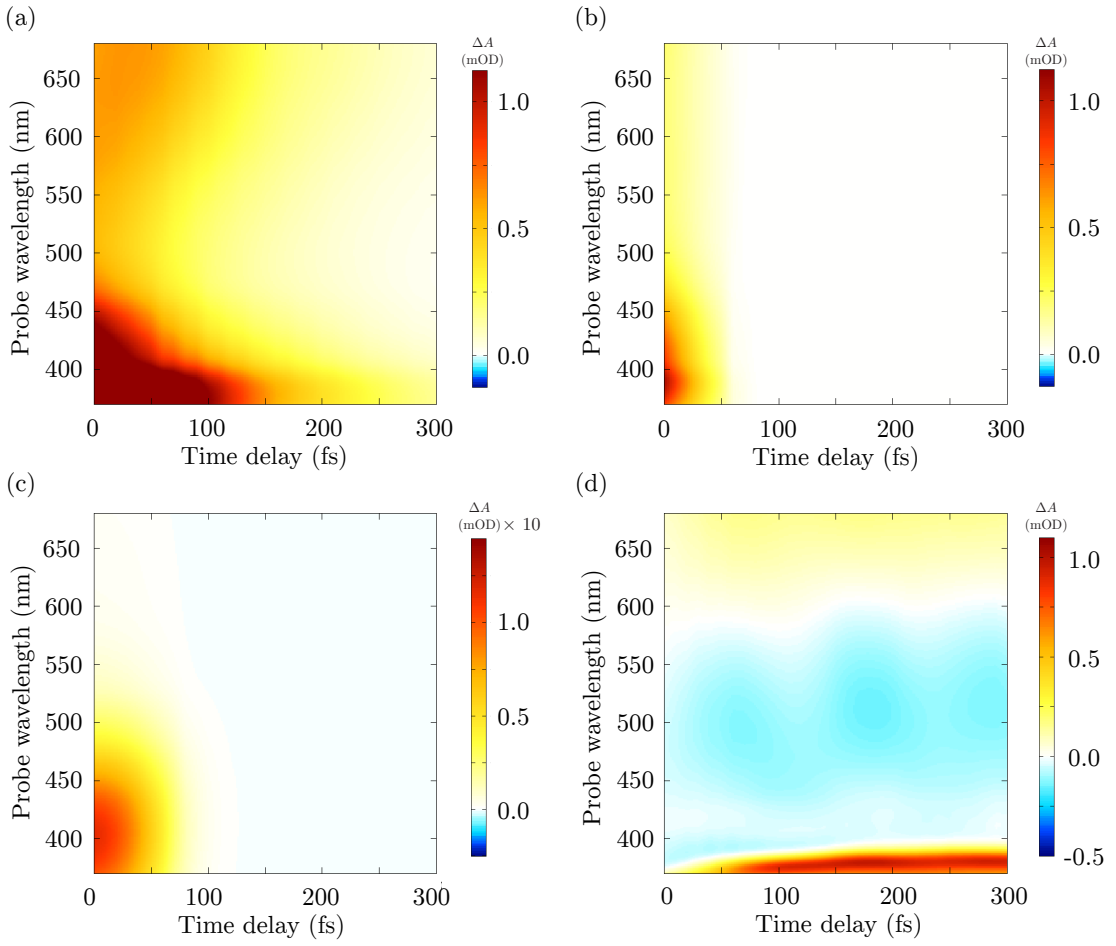

Figure 6.4: Individual contribution to the total computed PP map: (a) Contribution originated from the L_A state of the unfolded conformer. (b) Contribution originated form the L_A state of the folded conformer. (c) ESA signals arising from the CT state, the intensity scale has been multiplied by one order of magnitude. (d) Signals originated from the $\pi\pi^*$ state of nicotinamide. All these signals are computed employing a magic angle polarization between the *pump* and the *probe* pulse.

CT state (6.4-(c)) which is however one order of magnitude less intense compared to the other contributions. Moreover, this transition is covered by the ESA arising from the L_A state of the unfolded conformation (Fig. 6.4-(a)) which falls in the same spectral window. Giving a closer look to the other contributions one

clearly rationalize the origin of the long living ESA1 observed in the experiment as produced by the population of the $\pi\pi^*$ state of nicotinamide, supporting the hypothesis outlined in the previous section. By looking at Fig. 6.4-(d) one can also explain the origin of the long living ESA2 displayed by the experiment as again produced by the absorption of the $\pi\pi^*$ state of the acceptor. More in general, however, the scenario painted by the comparison of this individual contributions is that of a very congested spectral window where the signal produced by different valence states are strongly overlapping with each other.

6.5 Summary

In this chapter the photo-physics of the NADH dimer have been introduced. Experimental spectra have been presented a closer look was taken into the origin of the signals observed in the experiments disentangling also the contribution arising from folded and unfolded conformations of the system. In conclusion:

- Modeling the relaxation pathway of adenosine as a simple internal conversion towards the ground state is in agreement with experimental results. Morover, the DHO model employed to describe the dynamics of the system after the photo-excitation is able to account for the gross feature of the experimental spectra even if the static disorder of the system is neglected.

- Static disorder appears to be more important for the description of the long living ESA1 which is broader in the experiment compared to theory.

- Due to the large congestion in the UV-VIS window a direct observation of the CT is not possible since this signal is covered by the ESA contribution of the unfolded L_A state.

- For similar reasons, extracting the proper time-scale of the energy transfer is cumbersome due to the overlap between the unfolded L_A ESA and the $\pi\pi^*$ ESA. The buildup of the stimulated emission is also covered by other signals. This is similar to what discussed in Ref. [30] where an indirect measurement

based on a post-processing of the experimental data was performed in order to extract the ET rate.

We can conclude that, for a clear resolution of the energy transfer process in the NADH dimer, a different *time-resolved* technique is called for. In the next chapter we are going to investigate, with the help of theoretical simulations, different spectroscopic techniques with the aim of design an experiment capable of disentangling the different states populated after the light-matter interaction.

Chapter 7

Resolving the energy transfer process of NADH with ultrafast spectroscopy

7.1 Introduction

As we have already discussed in the last chapter, resolving the energy transfer process of NADH poses several challenges. The structural flexibility of the system leads to a conformational equilibrium between folded and unfolded conformations, with a preference for the unfolded state in water solution. Both the two conformers absorb light in the same spectral window, giving rise to a complex spectrum which is the combination of the individual signals arising from the two different conformational states. Folded and unfolded dimers exhibit different photo-physical behaviours: while the folded ones exhibit energy transfer, the unfolded conformers show a photo-physics which closely resemble that of the isolated adenonise nucleoside. When a PP experiment is performed in the optical regime, the fingerprints of the this two different channels are overlapped and difficult to disentangle, giving thus rise to a congested map which makes it difficult to completely resolve the energy transfer process. In this context it is highly desirable to design a technique capable of overcoming the aforementioned limitations.

Among the many well-established *time-resolved* electronic spectroscopic techniques, TR-PES has shown extreme sensitivity to both electronic and nuclear degrees of freedom[10], and the liquid microjet technology[11] has recently disclosed the possibility of applying such a technique in water solution. This advancement opened the possibility to perform experiments of more complex systems, such as molecular aggregates that only exists in salvation. The availability of this technological

improvement, combined with the well-established capabilities of TR-PES, makes it and intriguing candidate for studying the photo-physics of the NADH dimer.

The technological advancement has also impacted other windows of the spectrum: synchrotron light sources and X-ray free electron lasers[38] are disclosing a new era for the electronic spectroscopy[39]. The capabilities of X-ray based ultra-fast techniques have been successfully tested on a wide range of systems and of photo-physical processes. The capacity of these techniques ranges from: probing electronic coherences on the attosecond (as) to femtosecond (fs) time scales[40], revealing chemical reactions in real time[41], exploring spin-crossover dynamics[42] as well as change of electronic[43] and/or molecular structure in the excited state[44]. X-ray based techniques appear to be strong candidates for the resolution of the energy transfer process in NADH, even if the development of such techniques for ultra-fast X-ray spectroscopy is still ongoing.
On the one hand, the possibility to access new spectral windows and the corresponding spectroscopic techniques, opens up the possibility to study the same photo-physical process form different point of views. On the other ends, a clear understanding of which type of spectroscopy is more suited to capture a certain facade of a given photo-induced process is highly desired.
In this chapter, the ultrafst energy transfer in the NADH dimer will be simulated in different spectral windows, and the results of the various techniques will be placed in the context of the well-established *pump-probe* spectroscopy in the UV-VIS regime presented in the previous chapter. In particular the simulation of TR-PES, TR-NEXAFS and TR-XPS (on the nitrogen K-edge) techniques for the NADH dimer. Eventually, the obtained results will be used to establish which of these techniques is most suited for resolbing the photo-physical problem at hand.

7.2 Computational Methodology

The computational methodology used to evaluate the quantum chemical quantities of interest for the simulation of ultra-fast spectroscopy is here adapted according

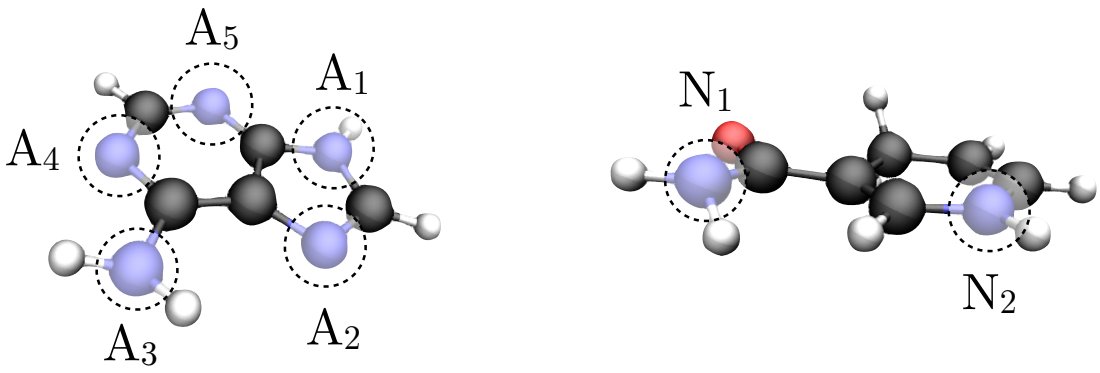

Figure 7.1: Labeling of the chemically different nitrogen atoms in the two moieties of the system. Nitrogen atoms of adenine are labeled as A_i, with i ranging from 1 to 5, while nitrogen atoms of nicotinamide are labeled as N_i, with $i = 1$ or $i = 2$.

to the three above mentioned techniques.

For the simulation of TR-PES, valence cationic states have to be computed. For the two distinct conformational states of the dimer this is achieved by means of the following CASSCF/CASPT2 calculations: for the unfolded conformer, an active space localized on the adenine moiety was designed, employing 4 doubly occupied π and 4 virtual π^* orbitals. The manifold of cationic states is then targeted by decreasing the number of active electrons to 7, and forcing the spin multiplicity to be 2. A SA-CASSCF calculation on 20 states was performed, and a perturbative correction to the energetics was calculated by means of the single state flavour of CASPT2. The same set of valence excited states computed in the previous chapter (for this conformation) can be used, and Dyson norms are obtained by means of the RASSI routine implemented in QC package OpenMolcas[27].
For the folded dimers, an active space composed by MOs belonging to both the two bases was designed. In particular, 4 doubly occupied (π) and 4 virtual (π^*) adenine orbitals were employed, together with 2 doubly occupied (π) and 2 virtual (π^*) nicotinamide orbitals. valence cationic states are thus computed with the same CASSCF/CASPT2 procedure explained above. The valence excited states required for the simulation of TR-PES are re-computed with the same active space

at the SA6-CASSCF level of theory and the XMS flavour of CASPT2 is applied on the top of the CASSCF wave-function.
The gradients of the cationic states required for the DHO model are obtained employing analytical differentiation at the CASSCF level of theory.

For the simulation of TR-NEXAFS, the calculation of core-excited states is required. Due to the element sensitivity displayed by the NEXAFS technique, the same process can be observed in three distinct X-ray windows, given by the carbon, nitrogen and the oxygen K-edges. Since carbon atoms are present also in the backbone of the system, signals on the carbon K-edge will incorporate contributions arising from these spectators atoms leading to a more congested spectrum. Similarly, oxygen is also present in the water molecules which surround the dimer: for this reason the oxygen K-edge signals of nicotinamide will be dominated by the intense response of the solvent. Nitrogen atoms, at variance, can be only found in the two bases, i.e. where the photo-induced dynamics takes place. Therefore, only the nitrogen K-edge of the system was simulated and is here reported. The NADH dimer is characterized by 7 chemically different nitrogen atoms (labeled in Fig. 7.1), 5 are located on the adenine moiety of the system while two are placed on the reduced nicotinamide. For the simulation of TR-NEXAFS, excitations starting from all of the 7 nitrogen atoms have to be included in the model. Obtaining the core excited state manifold in a single computation, will thus require to employ a large active space (including the 7 distinct N 1s orbitals an all the the MOs required for the proper description of the valence states in $|e\rangle$-manifold). Moreover, an enormous number of states would have to be included in the state average procedure to cover the entire NEXAFS spectrum. For this reason a commonly applied procedure in the field of X-ray spectroscopy simulations[45] is to split the core excited state calculation by computing the core excited states of each N individually.
As already discussed in the previous part of this thesis, core excited states are targeted by means of RASSCF calculations. TR-NEXAFS are therefore performed at the RASSCF/RASPT2 level of theory employing the following protocols for the

two distinct conformational states of the system:

- For the folded conformer, a minimum active space is designed to further speed up the calculation of core excited states. Seven separate calculation for each distinct nitrogen 1s orbitals are carried out employing the following AS: one nitrogen 1s orbital is placed in RAS1, allowing one hole to be created in this sub-space; the HOMO orbital for both adenine and nicotinamide ($H(A)$ and $H(N)$ respectively) are placed in RAS2; the LUMO orbitals of both the two bases ($L(A)$ and $L(N)$) are placed in RAS3, allowing up to 4 electrons to be placed in this sub-space. The HEXS[20] projection scheme is thus applied to RAS1, and the core excited states are computed within the CVS scheme. A Natural Transition Orbital (NTO) analysis[46], performed on a calculation employing a larger active space, reveals that both valence and core excited states are mainly described by a single electron excitations validating the use the a minimum active space here employed.
  The core excited state manifold for the folded conformer is then computed at SA-RASSCF level of theory including 10 state in the state average. Second order prturbative corrections are then computed on the top of the RASSCF wave-function, by means of the extended multi-state flavour of CASPT2 (XMS-CASPT2). In order to compute transition properties, the valence excited states of the $|e\rangle$-manifold are re-computed, with the same active space (but without employing the HEXS projection scheme), at the SA-RASSCF level of theory including 4 states in the state average and performing XMS-CASPT2 corrections. Excited state gradients are computed at the RASSCF level of theory by means of numerical differentiation. The same procedure is applied to all the 7 nitrogen 1s orbitals of the system.

- Core excited states of the unfolded conformer are computed at the same level of theory employing an AS composed by: one nitrogen 1s orbital in RAS1, the HOMO and the LUMO of adenine respectively in RAS2 and RAS3, allowing one hole in RAS1 and up to 2 electrons in RAS3. The HEXS projection scheme is applied to RAS1 and the core excited states are thus computed at the SA-RASSCF level including 2 states in the averaging

procedure. XMS-CASPT2 corrections on the top of the RASSCF solution were again considered. Valence excited states are then recomputed at the same level of theory without applaying the HEXS projection scheme.
Vertical gradients for core excited states of both folded and unfolded conformations are obtained at the RASSCF level by means of numerical differentiation.

For the simulation of TR-XPS, core cationic states have to be computed. This is practical achieved employing the same protocol explained above for TR-NEXAFS just considering the cationic speces instead of neutral states and forcing the spin multiplicity to be equal to 2. For both core excited and core ionized states transition dipole moments or Dyson norms are computed trough the RASSI routine of the QC package OpenMolcas[27].
Scalar relativistic effects were also taken into accounts via second order Douglass-Kroll-Hess Hamiltonian in combination with the ANO-RCC basis set[47, 48]. All the quantum chemical calculation discussed above were run with the QC package OpenMolcas via the COBRAMM interface[24].

7.3 Results and discussion

Before presenting the *time-resolved* techniques linear absorption/ionization signals are reported. The PES spectrum for the folded dimer conformation (showed in Fig. 7.2-(a)) exhibits 6 well resolved features in the binding energy window (BE) between 4 to 12 eV. The first two bands are produced by the ionization of nicotinamide frontier orbitals: the lowest energy band (ca. 5.00 eV) is associated to the ionization of the HOMO orbital of this moiety, while the second band, placed around 6.9 eV, is due to the ionization of the HOMO-1 of the same moiety. The BE region between 7 and 12 eV, at variance, presents a very rich structure: one can clearly identifies 4 well resolved bands which are mainly originated by the ionization of adenine frontier orbitals.

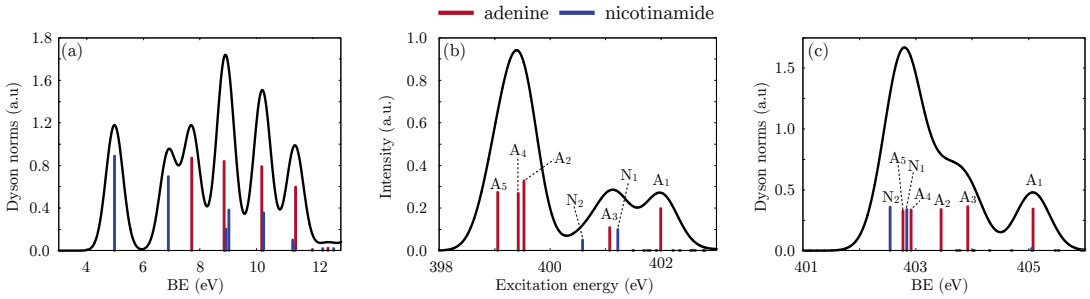

Figure 7.2: Linear absorption/ionization spectra of the folded NADH conformation. From *left* to *right*: (a) PES spectrum; (b) NEXAFS spectrum and (c) XPS spectrum. Signals are obtained employing a phenomenological Gaussian broadening of 0.3 eV which corresponds to a FWHM of ca. 0.7 eV. Contribution from the two different bases are depicted with different colors, in particular, blue sticks highlight excitations/ionizations localized on the nicotinamide moiety while red sticks highlight excitations/ionizations localized on adenine.

The nitrogen K-edge NEXAFS spectrum for the folded conformer presented in Fig. 7.2-(b) exhibits three resolved *pre*-edge features in the energy region between 398 and 403 eV. The first band, centered around 399.4 eV, is the combination of three electronic transitions from a 1s orbital to the LUMO orbital of the adenine moiety ($1s \rightarrow L(A)$) starting from three different nitrogen atoms. In particular, using the notation explained in figure 7.1 one can identify: the $1s(A_5) \rightarrow L(A)$ transition placed at around 399 eV; the $1s(A_4) \rightarrow L(A)$ transition at around 399.4 eV; and finally the $1s(A_2) \rightarrow L(A)$ at around 399.5 eV. By looking to the molecular structure of adenine (reported in figure 7.1) one can rationalize the energy position of these signals noticing that, the corresponding A_5, A_4 and A_2 nitrogen atoms are subjected to the same bound network (i.e, a $C-N$ double bond and a $C-N$ single bound) and thus they experience similar chemical environment. The band placed at ca. 401.2 eV is again due to the combination of three distinct core excitation, namely: $1s(N_2) \rightarrow L(N)$, $1s(A_3) \rightarrow L(A)$ and $1s(N_1) \rightarrow L(N)$, placed at 400.6, 401.1 and 401.3 eV respectively. These electronic transitions appear to be less intense compared to the those originated from A_5, A_4 and A_2 because $L(A)$ and $L(N)$ orbitals display less pronounced MOs coefficient over A_3, N_1 and N_2

atoms respectively. Finally the band located at around 402 eV, can be assigned to the $1s(A_1) \rightarrow L(A)$ transition.

The XPS spectrum at the N K-edge is reported in Fig. 7.2-(c). It exhibits a main band located at ca. 402.8 eV, characterized by a shoulder at around 403.9 eV, and a second band at around 405.1 eV. The first more intense band is produced by the combination of 4 core ionizations, namely: the $1s(N_2)$ ionization (402.6 eV) and three almost degenerate ionization signals (at ca. 402.8 eV) corresponding to the $1s(A_5)$, $1s(N_1)$ and $1s(A_4)$ ionizations. The shoulder observed around 403.9 eV is, at variance, produced by the $1s(A_2)$ and $1s(A_3)$ ionizations. Finally the band at around 403.9 eV, is due to the ionization of the $1s(A_1)$ orbital. By comparing the XPS and NEXAFS spectra one notices that the relative order of the signals is not preserved in the two spectra. In fact, the BE of the N_2 atoms appears to be lower compared to the nitrogen atoms of the adenine moiety, which however are characterized by lower excitation energies. This can be rationalized noticing that both excitation and binding energies depend also on the molecular orbital relaxation that occurs after the relocation/expulsion of a given core electron. The MOs relaxation process can be different for excitation (for which the electron is relocated in an empty molecular orbirtal) or ionization (for which it is extracted from the molecule), leading to a modified relative order of signals in XPS compared to NEXAFS.

7.3.1 *Time-resolved* techniques

The simulated TR-PES, TR-NEXAFS and TR-XPS spectra are presented and compared in figure 7.3. This facilitates the task of finding the best suited technique to resolve the energy transfer process in the NADH dimer.

Figure 7.3-(a) shows the computed TR-PES map. One clearly identify three main Excited State Ionization signals (ESI) in the BE window between 1.5 and 4.5 eV which is ca. 1 eV red shifted with respect to the lowest ground state ionization signal placed at 5.0 eV (and reported in figure 7.2-(a)). These signals are labeled

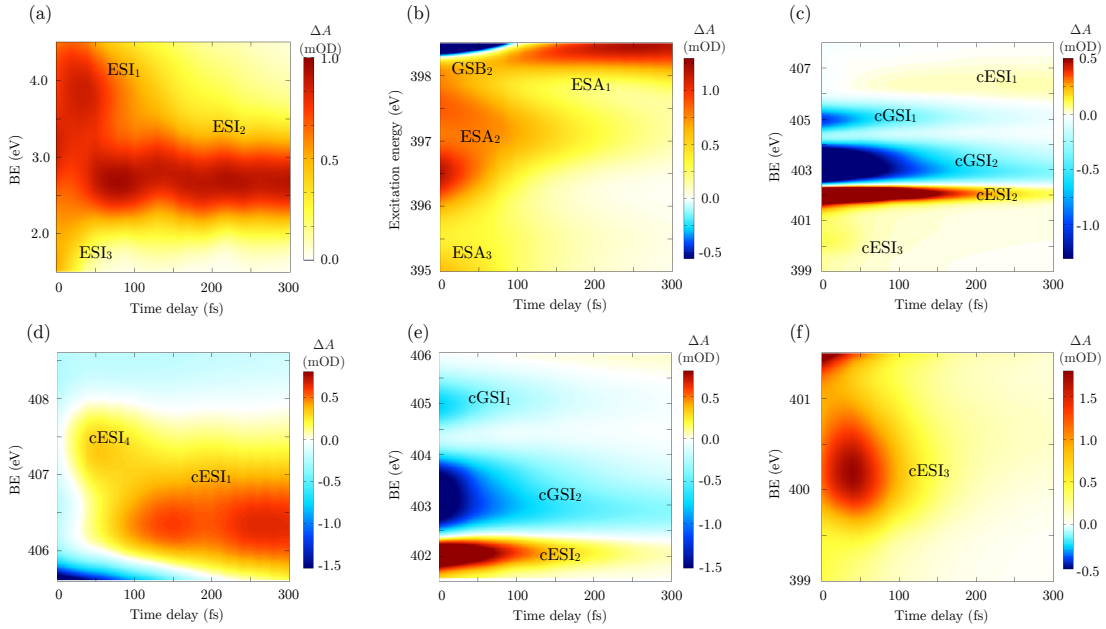

Figure 7.3: (a) TR-PES; (b) N K-edge TR-NEXAFS; (c) N K-edge TR-XPS spectra of the NADH dimer. The second row highlights different energy cuts of the total TR-XPS reported in (c). Individual contribution are labeled with the notation presented in the first part of the thesis. In particular, cESI is here used to label excited state ionizations involving core orbitals. Similarly cGSI refers to the ground state core ionization.

as ESI_1, ESI_2 and ESI_3 respectively. ESI_1 can be observed at early times at ca. 4.0 eV and displays an almost complete decay after 150 fs. This signal tracks the L_A to GS pathway observed for the unfolded state of NADH, and it is associated to the ionization of the adenine LUMO orbital (partially filled by the valence excitation). The electronic configuration of this cationic state can be written as $[H(A)^{(1)}]^+$ and it can be reached form the ground state by removing one electron from the $H(A)$ orbital. The corresponding ground state ionization is placed at ca. 7.9 eV as reported in Fig. 7.2-(a). The ESI_1 signal results 3.9 eV shifted compared to its corresponding GSI, allowing to resolve the L_A to GS deactivation pathway in a background free region. The energy position of this signal result in agreement with previous TR-PES experiments recorded on solvated adenosine[12]. ESI_2 con-

tribution, at variance, is placed at ca. 2.6 eV and shows a delayed increase that begins at around 50 fs and that persists for time longer than 300 fs. This signal can be assigned to the ESI of the nicotinamide $\pi\pi^*$ state. This is generated by the ionization of the $L(N)$ orbital which is partially filled in such state. Also this contribution has a GSI counterpart placed above the probed window, around 5.0 eV. Looking at these results one notices that TR-PES is able to clearly disentangle the signals arising from the folded state to these originated by unfolded conformation. In fact, ESI_2 appears to be red-shifted with respect to ESI_1 of ca. 1.4 eV allowing the direct observation of the population buildup in the $\pi\pi^*$ state during the ET process. This condition was not achievable with the UV-VIS *pump-probe* technique. Finally another ESI signal is observed around 1.6 eV which decays in around 50 fs. This signal (labeled as ESI_3) is due to the ionization of the L_A state of the folded NADH, and allows thus to track the population transfer between the L_A and the CT state. The latter, in particular, falls at the same BE of the folded L_A and for this reason the ESI_3 signal is actually the combination of the contributions arising from these two states. The L_A ionization, when the system is in the folded conformation, displays a red-shift of ca. 2.6 eV with respect to the corresponding ionization when the system is unfolded. This particular observation can be rationalized invoking the polarizative response of the other moiety which stabilize the cation in the folded state.

The TR-NEXAFS map, simulated at the nitrogen K-edge, is reported in Fig. 7.3-(b). This spectrum exhibits 4 distinct contributions in the probed energy window between 395 and 398.5 eV. Placed at ca. 398.3 eV, one identifies two different contributions with opposite sign: a negative signal labeled as GSB_2 and a positive signal labeled as ESA_1. GSB_2 can be observed at early times and decays after 100 fs. This signal is associated to the ground state bleaching of adenine in the unfolded conformation. ESA_2, at variance, shows a delayed buildup around 70 fs and it survives for more than 300 fs. One can easily assign this signal to the ESA of the $\pi\pi^*$ state of nicotinamide, allowing a direct tracking of the population in the final collector state of the ET. The intensity rise of ESA_1 in the TR-NEXAFS

spectrum, appear to be delayed with respect to the buildup of ESI_2 observed in the TR-PES due to the partial overlap with GSB_2. In the first 150 fs, the intensity of the GSB_2 contribution is decaying due to the ground state re-population after the L_A/GS internal conversion. At the same time, the ESA_1 increases in intensity due to the ultrafast energy transfer. The combination of these two opposite effects leads to an inversion time of about 70 fs where the ESA_1 signal became more intense than the GSB_2 contribution. The ESA_1 signal can be assigned to the core electronic transition $1s(N_2) \rightarrow L(N)$ (as the $L(N)$ orbital is partially filled in the $\pi\pi^*$ nicotinamide state). Around 396.5 eV the TR-NEXAFS spectrum exhibits anther ESA signal (labeled as ESA_2) which displays: a progressive time dependent blue-shift and an almost complete decay around 150 fs. One can clearly assign this signal to the ESA of the L_A state of the unfolded conformation. This signal is the combination of the $1s(A_5) \rightarrow L(A)$ and $1s(A_4) \rightarrow L(A)$ starting from the L_A state of adenine. Placed at lower excitations energies another ESA signal (ESA_3) is observed. It is characterized by a lower intensity, and it displays a spectral dynamics similar to that of ESA_2. ESA_3 is produced by the core electronic transition between the $1s(A_3)$ and the $H(A)$ orbital (which is accessible in the L_A state). No clear signatures of the CT state are observed.

The computed TR-XPS signal is presented in Fig. 7.3-(c). Compared to the other techniques the TR-XPS provides a more structured map concerning 5 different contributions. In the BE window between 399 and 408 eV one can clearly identify two GSI contributions placed at ca. 405 and 403 eV (respectively labeled as $cGSI_1$ and $cGSI_2$). Three different ESI contribution can be also found in the TR-XPS map, a more intense signal placed at ca. 402 eV ($cESI_2$) and two weaker contributions at around 406.5 ($cESI_1$) and 400 eV ($cESI_4$). By dividing the BE window probed in fig. 7.3-(c) in different sub-regions, one can extract a detailed picture of the NADH photo-induced dynamics. The total BE window is divided in: (i) an upper region between 405.5 and 408 eV; (ii) a central region between 401.5 and 406 eV; (iii) a lower region between 399 and 401.5 eV. The three TR-XPS maps corresponding to these different sub-windows are reported in fig. 7.3 from

(d) to (f). By looking at 7.3-(d), one is able to identify an additional weak ESI signal placed at ca. 407.5 eV ($cESI_4$) which displays a buildup around 25 fs and a subsequent decay around 100 fs. One can easily assign such signal to the $1s(N_2)$ ionization starting from the CT state. $cESI_1$, at variance, is placed at ca. 406.3 eV and shows a delayed buildup around 50 fs. This signal can be assigned to the $1s(N_2)$ ionization of the $\pi\pi^*$ collector state of nicotinamide. In contrast to what was observed in the previous simulations, TR-XPS is able to clearly resolve the various components of the ET process. In particular, one can clearly identify fingerprints of the CT state which are otherwise inaccessible to the other spectra windows/techniques.

Looking at the BE window between 401.5 and 406 (reported in figure 7.3-(e)) one can identify three main signals labeled as $cGSI_1$, $cGSI_2$ and $cESI_2$. These contributions are generated by the background signal of the NADH ground state and they resemble the profile showed in fig. 7.2-(c). These signals display a decay after ca. 150 fs which is almost complete for $cGSI_1$ while a constant intensity is reached for $cGSI_2$. The cESI centered at ca. 402 eV ($cESI_2$), at variance, shows an almost complete decay with the same time-scale. The spectral dynamics of the GSI contributions is due to the adenine ground state re-population after the L_A/GS internal conversion and after the energy transfer. The intensity plateau reached by $cGSI_2$ is assigned to the $1s(N_1)$ and $1s(N_2)$ ionization of the nicotinamide ground state. The $cESI_2$ contribution is the combination of $1s(A_4)$ and $1s(A_5)$ ionization of the L_A state of the unfolded, conformer and for this reason the spectral dynamics of such signal is capable of tracking the L_A/GS internal conversion. Ionization of nitrogen atoms from A_1 to A_3 are in contrast covered by the $cGSI_2$ contribution. The TR-XPS signals placed in this BE window are thus perfectly suited to resolve the photo-physics of the unfolded state of the dimer.

The BE sub-region between 399 and 401.5 eV (reported in Fig. 7.3-(f)) exhibits only one ESI contribution, characterized by a delayed buildup around 25 fs followed by an almost complete decay after 100 fs. This signal displays the same character showed by the $cESI_4$ contribution and can be assigned to the CT state ionization. In particular, this signal is produced by the combination of $1s(A_3)$, $1s(A_4)$ and

$1s(A_5)$ ionization of the CT state. This signal appears in a background free region red-shifted of ca. 3.0 eV with respect to the cGSI energy region. The population dynamics of the CT state can therefore be resolved, in this energy window, without any interference of other signals.

Compered with other *time-resolved* techniques, TR-XPS is able to spread the signal associated to different *valence*-excited states on a large BE window, enabling the disentanglement of the different photo-physical paths that occurs after the optical excitation. In particular, TR-XPS displays high sensitivity to the CT state, which give rise to two distinct fingerprints namely the blue-shifted $cESI_4$ and the red-shifted $cESI_3$. Starting from this results one can conclude that TR-XPS is the technique of choice for resolving the ET process in the NADH dimer.
In the following section the excited state chemical shifts displayed by the TR-XPS experiments are analyzed in depth, and a theoretical model able to rationalize them is proposed.

7.3.2 Excited-state chemical shift in TR-XPS: an electrostatic model

The BE energy of a given core orbital is highly influenced by the local chemical environment. This argument, is well known since the fist observation by Kai M. Siegbahn[49] awarded with the Nobel prize in physics in 1981. This sensitivity is typically explained considering the electron density residing over the ionized X-ray cromophore (i.e, the nitrogen atoms in our case). In fact, ionizing a site of the system where the electron density is more localized, requires less energy compared to the ionization of a neutral or partially positive center of the molecule. This simple electrostatic rational can be straightforwardly applied to the excited-state chemical shifts. In particular, one realizes that different optically excited states are characterized by different electron density distribution leading to different TR-XPS fingerprints. Moreover, during the photo-induced dynamics initiated by an optical *pump*, the coupled electron-nuclear motion of the system can perturb the electron density distribution allowing for a time dependent modification of the

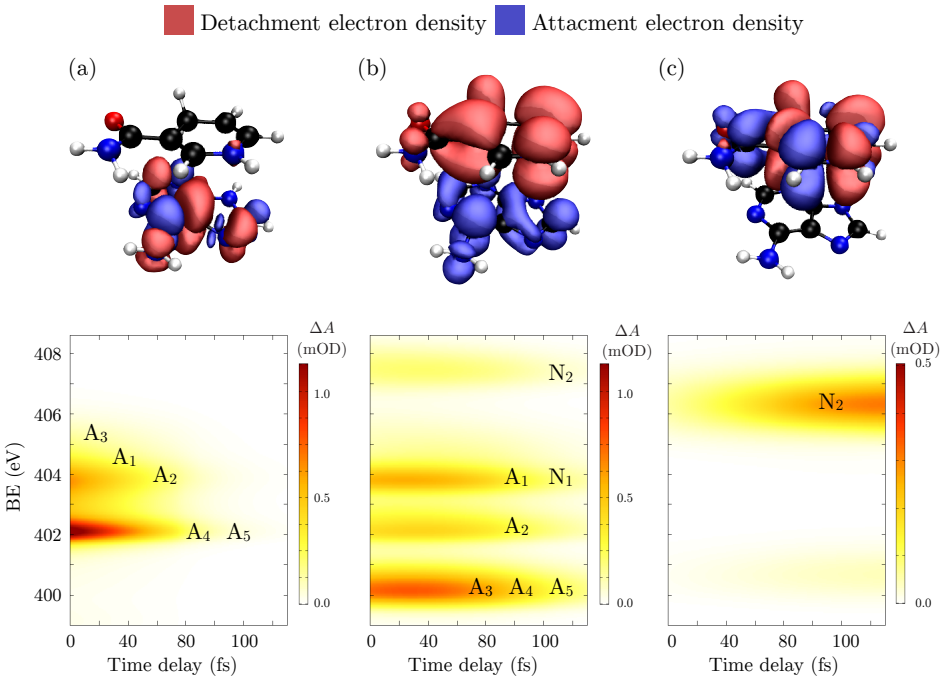

Figure 7.4: Rationalization of the excited state chemical shifts observed in TR-XPS. *Top*: difference between attachment and detachment electron density for the L_A (a), CT (b) and $\pi\pi^*$ (c) states of the folded NADH conformation. Red iso-surfaces highlight the detachment density, while the attachment density is depicted with blue iso-surfaces. *Bottom*: Excited state core ionization computed for the L_A (a), CT (b) and $\pi\pi^*$ (c) states of NADH in the same conformation. The nomenclature reported in Fig. 7.1 is here used to label the individual contributions of different nitrogen 1*s* orbitals.

TR-XPS chemical shifts. To understand the relative BE of the signals collected in Fig. 7.3-(c), for each one of the *valence*-excited states considered (i.e: L_A, CT, $\pi\pi^*$), the difference between attachment and detachment density[46] is invoked. For a given electronic excitation the latter evaluates where the electron density of the system is drained while the former describes where it is relocated after the excitation process. The difference between these two electron density distributions was obtained by means of transition density analysis[46] and they are reported in figure 7.4 (a), (b) and (c) for the aforementioned electronic states of the NADH

dimer.

Looking at the electron density distribution over the nitrogen atoms of the system in the L_A state, one notes that the electron density over A_4 and A_5 is increased. This leads to a redshift of ca. 0.8 eV of both $1s(A_4)$ and $1s(A_5)$ ionizations as observed in the TR-XPS map reported in figure 7.3-(e) and depicted in 7.4-(a). The electron density over A_2 and A_3 is on the contrary decreased leading to a blue-shift of 0.5 and 0.8 eV respectively. Electronic density over A_1 is almost untouched leading only to a minor 0.1 eV of shift.

Similarly the electronic density over N_2 in the $\pi\pi^*$ state of nicotinamide is highly decreased leading to strong blue-shift of the $1s(N_2)$ ionization of ca. 4 eV. N_1, on the contrary, is exposed to almost the same electronic density in the ground and in the $\pi\pi^*$ state and thus its chemical shift is unaffected. However, this signal exhibit a lower intensity with respect to other signals and for this reason it is not visible in the spectra reported in Fig. 7.4-(c). The low intensity signal observed around 400 eV and reported in figure 7.4-(c) is associated to a shake down satellite and thus it displays an intensity which is an order of magnitude lower compared to main signal at ca. 406.3 eV.

In the CT state an electron is transferred from the nicotinamide moiety to the adenine one, with a consequent charge separation between the two bases. Following the electrostatic model considered until now, one realizes that removing on electron from adenine (which is negatively charged) requires less energy compared to the detachment of an electron from the niconitamide moiety of the system (since it is positively charged). This observation explains why the CT fingerprints, in the TR-XPS spectrum, are associated to both a red-shift of the adenine core ionizations and a blue-shift of nicotinamide core ionizations. Very importantly, we note that these considerations are not system dependent and therefore similar reasoning can be invoked every time a clear charge separation (due to molecular excitation) is observed. For these reasons, TR-XPS appears to be the technique of choice to monitor the population dynamics of *intra* or *inter*-molecular CT in generic systems.

On a final note, we observe that in the NADH dimer the negative (positive) charge

in the CT state is not equally distributed over the molecular system. This leads to different nitrogen chemical shifts according to the electronic density located over the ionized center: since larger electronic density can be found over A_3, A_4 and A_5 atoms this leads to a strong red-shift of the corresponding $1s$ ionization of ca. 3.0, 2.8 and 2.8 eV, respectively. Only a smaller amount of electronic density is relocated on A_2 and A_1, which in fact exhibit a less pronounced red-shift of ca. 1.8 eV and 1.2 eV. This opens the possibility to experimentally resolve the charge distribution in the CT state with a (partial) atomic resolution, allowing to gain structural insights upon where the surpluss of negative charge is located in the molecular system (i.e, over the six member ring in this case). Unfortunately, these last two signals are for the NADH dimer covered by ESI_2 and by GSI_2 contributions produced by the unfolded conformer, and they are thus not visible in the total spectra. Similarly, the electron hole in the nicotinamide moiety leads to a pronounced decreasing of the electronic density over the N_2 center which translates into an equally pronounced blue-shift of ca. 4.5 eV. A smaller amount of electronic density is drained by the external N_1 site, which exhibits only a minor blue-shift of 0.8 eV.

7.4 Summary

The simulations of TR-PES, N K-edge TR-NEXAFS and N K-edge TR-XPS of the NADH dimer in water solution were presented. These were obtained by means of a computational protocol based on multi-reference wave-function theory (CASSCF/ CASPT2 and RASSCF/RASPT2) methods which is able to describe states of very different nature (core excited and valence/core ionized states) at equal footing. The outcomes of the simulations are compared and the capabilities of each of these techniques in the resolution of the ET process was compared. TR-PES and TR-NEXAFS are shown to provide clear information about the buildup of the population in the final $\pi\pi^*$ state of nicotinamide (a clear signature of the energy transfer process), but both are almost blind to the population dynamics in the CT state. The signals of different conformations (i.e, the folded and the unfolded

states of the dimer) are well separated in both TR-PES and TR-NEXAFS allowing to disentangle the spectral dynamics produced by the L_A/GS internal conversion from the that associated to the ET process. TR-XPS, at variance, shows a more structured map which allows to completely resolve the energy transfer process. In particular, the total BE window probed in TR-XPS have been divided in three regions: an upper window between 405.5 and 408.5 eV which enables to study the ET transfer process without any background produced by the unfolded conformers; a central window, between 401.5 and 406 eV, where the internal conversion of the unfolded conformers can be tracked; an lower BE region, between 399 and 401.5 eV, which can be used to monitor the population dynamics of the CT state without any background signal.

Finally the origin of the chemical shifts observed in TR-XPS were are rationalized correlating them with the electron density distribution of the three different states involved in the model. The capability of TR-XPS to resolve the CT state have been also discussed, and the trasferability of the proposed analysis to other molecular systems is also discussed. In conclusion, TR-XPS results to be the technique of choice for resolving the energy transfer process in the NADH dimer providing a detailed picture of the photo-induced dynamics. Eventually, this the technique showed enough atomic resolution to probe locally the charge distribution of different *valence*-excited states providing structural information otherwise inaccessible in other ionization techniques such as TR-PES.

Chapter 8

Appendix: Active spaces

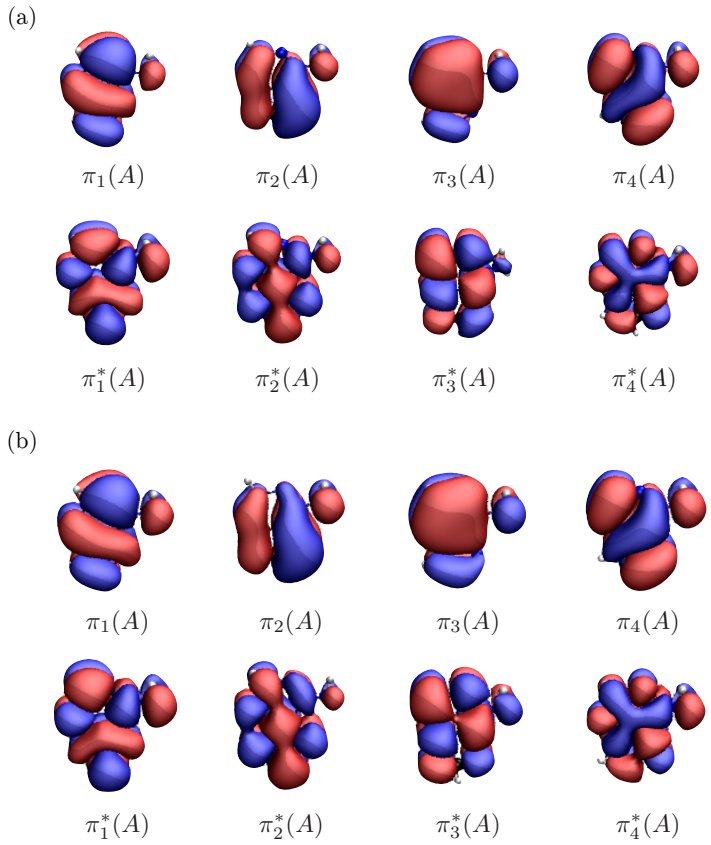

Figure 8.1: (a) AS employed in the calculation of valence excited states of the unfolded dimers. (b) AS employed in the calculation of cationic states of the unfolded conformer.

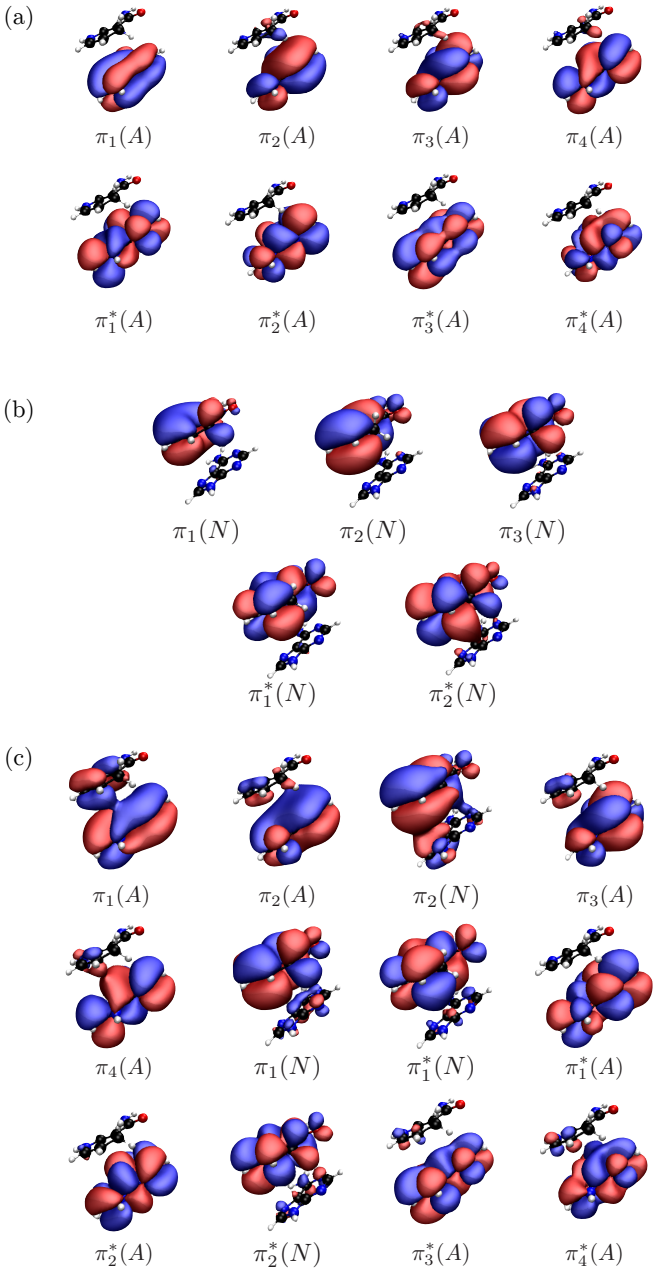

Figure 8.2: (a) AS employed in the calculation of adenine valence excited states in the folded conformers of NADH. (b) AS employed in the calculation of nicotinamide valence excited states in the folded conformations of NADH. (c) AS employed in the calculation of the ESA contributions of the CT state.

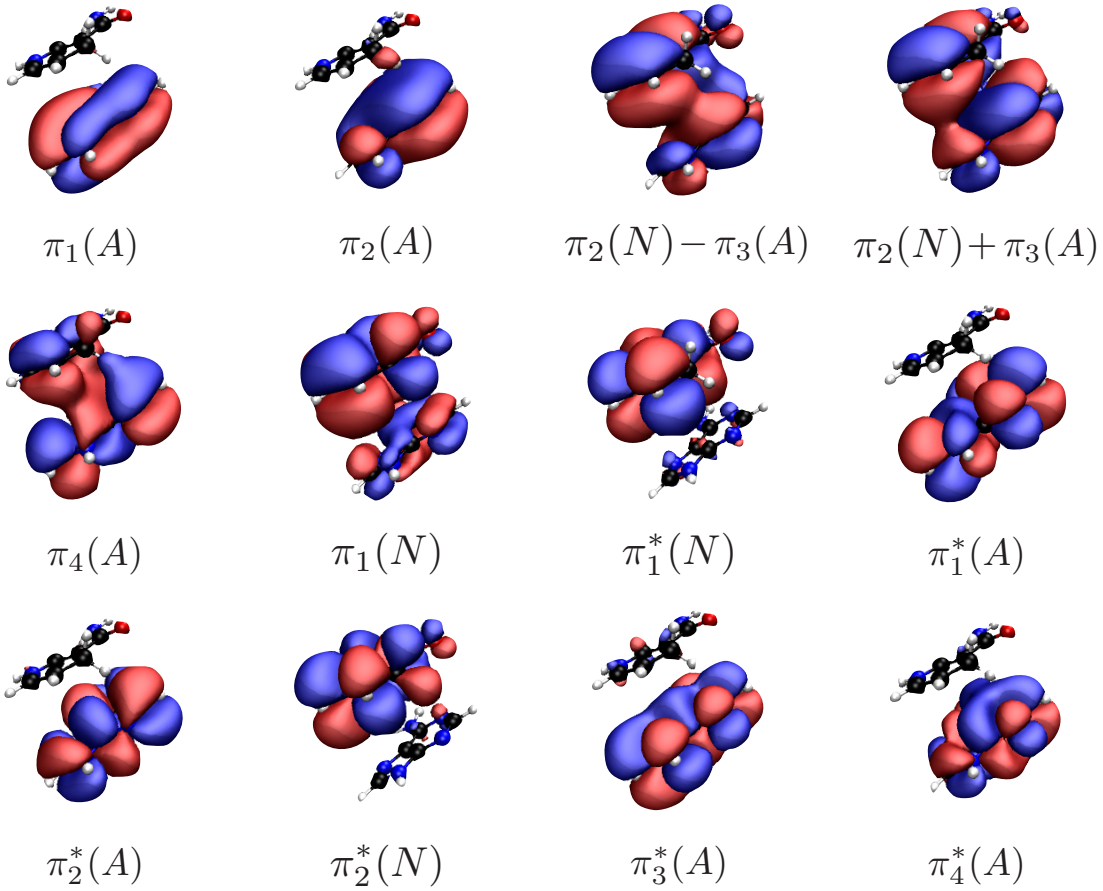

Figure 8.3: AS employed in the calculation of the cationic states for the folded dimers.

Chapter 9

Conclusions

In this thesis the problem of simulating ultrafast spectroscopy is presented and the complementarity of different spectroscopic techniques is discussed on a specific example, namely, the photo-induced dynamics of the NADH dimer. Two main theoretical pillars have been discussed in this thesis: the phenomenological and theoretical description of electronic spectroscopy (Part I) and the first-principles computation of quantum mechanical properties of molecular systems embedded in a complex environments, with particular attention to the properties of core-excited states (Part II).

The former task has been archived by means of the perturbative response function approach, while the later has been tacked employing the multireference perturbative CASSCF/CASPT2 or RASSCF/RASPT2 methodology. These concepts have been applied to answer a specific question: which is the best spectroscopic technique to resolve the energy transfer process between the adenine and nicotinamide moieties of the NADH dimer?

Starting from mechanistic insights, obtained by a quantum dynamical study, different ultrafast spectroscopic techniques have been simulated. The simulated spectra have been eventually compared, to establish which of these techniques was best suited to describe the process of interest. In particular UV-VIS *pump-probe*, TR-PES, N K-edge TR-NEXAFS and TR-XPS have been simulated and benchmarked in this thesis.

By comparing the simulated UV-VIS *pump-probe* spectra with the recently recorded experimental counterpart, the role of the conformation flexibility of the system have been discussed. The results obtained by previous experimental investigation of the ET process in NADH were critically considered, and the difference between theory and experiment has been carefully highlighted.

By comparing TR-PES, TR-NEXAFS and TR-XPS, the technique of choice for resolving the ET process in NADH has been identified. TR-XPS has shown astonishing capabilities in the resolution of the ET process, allowing for a clear disentanglement of all the photo-induced pathways occurring when NADH is excited.

The capabilities of this technique have been eventually rationalized employing a simple, but robust, electrostatic model. Finally, the generality of these consideration suggests the possibility to use TR-XPS as a general tool for resolving the population dynamics of charge transfer states for a large variety of systems.

Bibliography

(1) Polli, D.; Altoè, P.; Weingart, O.; Spillane, K. M.; Manzoni, C.; Brida, D.; Tomasello, G.; Orlandi, G.; Kukura, P.; Mathies, R. A.; Garavelli, M.; Cerullo, G. *Nature* **2010**, *467*, 440–443.

(2) Collini, E.; Wong, C. Y.; Wilk, K. E.; Curmi, P. M. G.; Brumer, P.; Scholes, G. D. *Nature* **2010**, *463*, 644–647.

(3) Segatta, F.; Cupellini, L.; Garavelli, M.; Mennucci, B. *Chemical Reviews* **2019**, *119*, 9361–9380.

(4) Conti, I.; Cerullo, G.; Nenov, A.; Garavelli, M. *Journal of the American Chemical Society* **2020**, *142*, 16117–16139.

(5) Abramavicius, D.; Palmieri, B.; Voronine, D. V.; anda, F.; Mukamel, S. *Chemical Reviews* **2009**, *109*, 2350–2408.

(6) Keefer, D.; Aleotti, F.; Rouxel, J. R.; Segatta, F.; Gu, B.; Nenov, A.; Garavelli, M.; Mukamel, S. *Proceedings of the National Academy of Sciences* **2021**, *118*, DOI: 10.1073/pnas.2022037118.

(7) Keefer, D.; Schnappinger, T.; de Vivie-Riedle, R.; Mukamel, S. *Proceedings of the National Academy of Sciences* **2020**, *117*, 24069–24075.

(8) Nam, Y.; Montorsi, F.; Keefer, D.; Cavaletto, S. M.; Lee, J. Y.; Nenov, A.; Garavelli, M.; Mukamel, S. *Journal of Chemical Theory and Computation* **2022**, *18*, 3075–3088.

(9) Neville, S. P.; Chergui, M.; Stolow, A.; Schuurman, M. S. *Physical Review Letters* **2018**, *120*, DOI: 10.1103/physrevlett.120.243001.

(10) Stolow, A.; Bragg, A. E.; Neumark, D. M. *Chemical Reviews* **2004**, *104*, 1719–1758.

(11) Suzuki, T. *The Journal of Chemical Physics* **2019**, *151*, 090901.

(12) Buchner, F.; Ritze, H.-H.; Lahl, J.; Lübcke, A. *Physical Chemistry Chemical Physics* **2013**, *15*, 11402.

(13) Segatta, F.; Nenov, A.; Orlandi, S.; Arcioni, A.; Mukamel, S.; Garavelli, M. *Faraday Discussions* **2020**, *221*, 245–264.

(14) Segatta, F. **2018**, DOI: 10.6092/UNIBO/AMSDOTTORATO/8469.

(15) Bennett, K.; Kowalewski, M.; Mukamel, S. *Faraday Discussions* **2015**, *177*, 405–428.

(16) Pitea, T.; Sapunar, M.; Ponzi, A.; Gelin, M. F.; Doli, N.; Domcke, W.; Decleva, P. *Journal of Chemical Theory and Computation* **2021**, *17*, 5098–5109.

(17) Grell, G.; Bokarev, S. I. *The Journal of Chemical Physics* **2020**, *152*, 074108.

(18) Bartlett, R. J. *Annual Review of Physical Chemistry* **1981**, *32*, 359–401.

(19) Pople, J. A.; Seeger, R.; Krishnan, R. *International Journal of Quantum Chemistry* **2009**, *12*, 149–163.

(20) Delcey, M. G.; Sørensen, L. K.; Vacher, M.; Couto, R. C.; Lundberg, M. *Journal of Computational Chemistry* **2019**, *40*, 1789–1799.

(21) Reiher, M. *Theoretical Chemistry Accounts* **2006**, *116*, 241–252.

(22) Battaglia, S.; Lindh, R. *Journal of Chemical Theory and Computation* **2020**, *16*, 1555–1567.

(23) Grell, G.; Bokarev, S. I.; Winter, B.; Seidel, R.; Aziz, E. F.; Aziz, S. G.; Kühn, O. *The Journal of Chemical Physics* **2015**, *143*, 074104.

(24) Avagliano, D.; Bonfanti, M.; Garavelli, M.; González, L. *Journal of Chemical Theory and Computation* **2021**, *17*, 4639–4647.

(25) Segatta, F.; Nenov, A.; Nascimento, D. R.; Govind, N.; Mukamel, S.; Garavelli, M. *Journal of Computational Chemistry* **2021**, *42*, 644–659.

(26) Moca, R.; Meech, S. R.; Heisler, I. A. *The Journal of Physical Chemistry B* **2015**, *119*, 8623–8630.

(27) Aquilante, F. et al. *The Journal of Chemical Physics* **2020**, *152*, 214117.

(28) WEBER, G. *Nature* **1957**, *180*, 1409–1409.

(29) Hull, R. V.; Conger, P. S.; Hoobler, R. J. *Biophysical Chemistry* **2001**, *90*, 9–16.

(30) Heiner, Z.; Roland, T.; Leonard, J.; Haacke, S.; Groma, G. I. *The Journal of Physical Chemistry B* **2017**, *121*, 8037–8045.

(31) Aleotti, F.; Aranda, D.; Jouybari, M. Y.; Garavelli, M.; Nenov, A.; Santoro, F. *The Journal of Chemical Physics* **2021**, *154*, 104106.

(32) Bai, S.; Barbatti, M. *Journal of Chemical Theory and Computation* **2019**, *15*, 1503–1513.

(33) Roy, A.; Hua, D. P.; Ward, J. M.; Post, C. B. *Journal of Chemical Theory and Computation* **2014**, *10*, 2759–2768.

(34) Cadena-Caicedo, A.; Gonzalez-Cano, B.; López-Arteaga, R.; Esturau-Escofet, N.; Peon, J. *The Journal of Physical Chemistry B* **2019**, *124*, 519–530.

(35) Conti, I.; Garavelli, M.; Orlandi, G. *Journal of the American Chemical Society* **2009**, *131*, 16108–16118.

(36) Tuna, D.; Sobolewski, A. L.; Domcke, W. *The Journal of Physical Chemistry A* **2013**, *118*, 122–127.

(37) Chatterley, A. S.; West, C. W.; Roberts, G. M.; Stavros, V. G.; Verlet, J. R. R. *The Journal of Physical Chemistry Letters* **2014**, *5*, 843–848.

(38) McNeil, B. W. J.; Thompson, N. R. *Nature Photonics* **2010**, *4*, 814–821.

(39) Kraus, P. M.; Zürch, M.; Cushing, S. K.; Neumark, D. M.; Leone, S. R. *Nature Reviews Chemistry* **2018**, *2*, 82–94.

(40) Goulielmakis, E.; Loh, Z.-H.; Wirth, A.; Santra, R.; Rohringer, N.; Yakovlev, V. S.; Zherebtsov, S.; Pfeifer, T.; Azzeer, A. M.; Kling, M. F.; Leone, S. R.; Krausz, F. *Nature* **2010**, *466*, 739–743.

(41) Attar, A. R.; Bhattacherjee, A.; Pemmaraju, C. D.; Schnorr, K.; Closser, K. D.; Prendergast, D.; Leone, S. R. *Science* **2017**, *356*, 54–59.

(42) Bressler, C.; Milne, C.; Pham, V.-T.; ElNahhas, A.; van der Veen, R. M.; Gawelda, W.; Johnson, S.; Beaud, P.; Grolimund, D.; Kaiser, M.; Borca, C. N.; Ingold, G.; Abela, R.; Chergui, M. *Science* **2009**, *323*, 489–492.

(43) Wolf, T. J. A. et al. *Nature Communications* **2017**, *8*, DOI: 10.1038/s41467-017-00069-7.

(44) van der Veen, R.; Milne, C.; El Nahhas, A.; Lima, F.; Pham, V.-T.; Best, J.; Weinstein, J.; Borca, C.; Abela, R.; Bressler, C.; Chergui, M. *Angewandte Chemie* **2009**, *121*, 2749–2752.

(45) Montorsi, F.; Segatta, F.; Nenov, A.; Mukamel, S.; Garavelli, M. *Journal of Chemical Theory and Computation* **2022**, *18*, 1003–1016.

(46) Plasser, F.; Wormit, M.; Dreuw, A. *The Journal of Chemical Physics* **2014**, *141*, 024106.

(47) Almlöf, J.; Taylor, P. R. *The Journal of Chemical Physics* **1987**, *86*, 4070–4077.

(48) Roos, B. O.; Lindh, R.; Malmqvist, P.-Å.; Veryazov, V.; Widmark, P.-O. *The Journal of Physical Chemistry A* **2005**, *109*, 6575–6579.

(49) *Philosophical Transactions of the Royal Society of London. Series A, Mathematical and Physical Sciences* **1970**, *268*, 33–57.